Properties of traveling ionospheric disturbances (TIDs) over the Western Cape, South Africa

A thesis submitted in fulfilment of the

requirements for the degree of

MASTERS IN SCIENCE

of

RHODES UNIVERSITY

by

VUMILE MIKE TYALIMPI

April 2014

Abstract

Travelling Ionospheric Disturbances (TIDs) are said to be produced by atmospheric gravitational waves propagating through the neutral ionosphere. These are smaller in amplitude and period when compared to most ionospheric disturbances and hence more difficult to measure. Very little is known about the properties of the travelling ionospheric disturbances (TIDs) over the Southern Hemisphere regions since studies have been conducted mostly over the Northern Hemisphere regions. This study presents a framework, using a High Frequency (HF) Doppler radar to investigate the physical properties and the possible driving mechanisms of TIDs. This research focuses on studying the characteristics of the TIDs, such as period, velocity and temporal variations, using HF Doppler measurements taken in South Africa. By making use of a Wavelet Analysis technique, the TIDs' characteristics were determined. A statistical summary on speed and direction of propagation of the observed TIDs was performed. The winter medium scale travelling ionospheric disturbances (MSTIDs) observed are generally faster than the summer MSTIDs. For all seasons, the MSTIDs had a preferred south-southwest direction of propagation. Most of the large scale travelling ionospheric disturbances (LSTIDs) were observed during the night and of these, the spring LSTIDs were fastest when compared to autumn and summer LSTIDs. The general direction of travel of the observed LSTIDs is south-southeast. Total Electron Content (TEC), derived from Global Positioning System (GPS) measurements, were used to validate some of the TID results obtained from the HF Doppler data. The Horizontal Wind Model (HWM07), magnetic K index, and solar terminators were used to determine the possible sources of the observed TIDs. Only 41% of the observed TIDs were successfully linked to their possible sources of excitation. The information gathered from this study will be valuable in future radio communications and will serve as means to improve the existing ionospheric models over the South African region.

Acknowledgments

I would like to thank the following people for supporting and assisting me during my candidature.

My supervisors, Dr Lee-Ann McKinnell and Dr Zama T. Katamzi, South African National Space Agency for their technical guidance and support.

Dr Jaroslav Chum, SANSA HF Doppler radar expect from Czech republic, for providing me with initial softwares and support.

The South African National Space Agency (SANSA) for providing me with funding and researching utilities.

Rhodes University for giving me the opportunity to undertake this study.

My parents and brothers for their endless love, unwavering support and encouragement.

Friends and very dear friends for their backing.

SANSA colleagues as they made my stay here worthwhile.

Last but not least, my son, Liyolatha Oyintanda Tyalimpi as he was very inspirational to me.

Contents

List of Figures

List of Tables

Chapter 1

Introduction

The ionosphere is defined, by Rishbeth and Garriott (1969), to be the part of the Earth's upper atmosphere where ions and electrons are present in quantities sufficient enough to affect the propagation of a radio wave. The ionosphere is a highly variable and conducting region of the atmosphere, and since 1901 it has not been understood that radio wave communication systems rely on the reflective properties of the ionosphere (Rawer, 1993, p. 4). Therefore the understanding of the dynamics of the ionosphere is a core part of radio communication as this medium reflects and refracts radio signals. High frequency (HF) radio waves are electromagnetic waves in the frequency range of $3 - 30$ MHz in the radio spectrum (Davies, 1989, p. 3). HF communication has been successfully demonstrated as a means for wireless communication with many advantages including low cost, mobility and robustness. This has since fuelled the electromagnetic probing of the ionosphere in an attempt to understand both its nature and dynamics.

Atmospheric gravity waves (AGW) in the neutral atmosphere have been studied theoretically and experimentally for many years (refer to Hines, 1960; Hodges, 1967; Cowling et al., 1971; Hunsucker, 1982; Chane-Ming et al., 2003). Historical studies of travelling ionospheric disturbances (TIDs) mainly linked them to meteorological sources (for e.g. Munro, 1950; Price, 1953; Munro, 1958). It was the realization that TIDs were the manifestation of gravity waves that led in part to the seminal paper by Hines (1960) whose pioneering work also helped establish the importance of wave transfer of energy and momentum from the lower to the middle and upper atmosphere. In the interim more recent studies have discovered a wider variety of TIDs' sources (refer to Georges, 1968; Cheng et al., 1997; He and Dyson, 2002;

MacDougall and Jayachandran, 2011).

A variety of ionospheric sounding techniques such as ionosondes, GPS satellites, radio interferometry, Super Dual Auroral Radar Network (SuperDARN) and incoherent scatter radars, have been utilized to study the ionosphere and ionospheric perturbations such as TIDs (for e.g. Hajkowicz, 1990; Afraimovich et al., 1998; Galushko and Paznukhov, 1998; He and Dyson, 2002). However, a HF Doppler radar was used in this study because of its advantages over other sounders such as relatively low cost, low output power, better time resolution and sensitivity to small perturbations in the ionosphere. The South African Western Cape radar network has a quasi-isosceles configuration made out of three transmitters which are located in Arniston ($34^{\circ}36'9''S$, $20^{\circ}18'10''E$), Cape Town ($33^{\circ}56'16''S$, $18^{\circ}28'15''E$) and Worcester ($33^{\circ}38'42''S$, $19^{\circ}26'37''E$), with one receiver located in Hermanus ($34^{\circ}25'30''S$, $19^{\circ}13'30''E$).

1.1 Objectives of the study

This study was conducted with an aim of understanding the nature and the origins of TIDs over the South African region using a HF Doppler radar. The main aim was divided into the following objectives:

- Identify TIDs using the HF Doppler radar and determine their propagation characteristics namely; the speed, period, wavelength and direction of propagation.
- Provide statistical information of TIDs' propagation properties such as spatial and temporal dependances.
- Determine the possible sources and driving mechanisms of the observed TIDs.

The outcomes from this study will contribute to our knowledge of the dynamics of the ionized atmospheric plasma and help develop TIDs' models with the main purpose of improving HF radio communication over South Africa.

1.2 Background Theory

1.2.1 Earth's Atmosphere

The Earth's atmosphere is a combination of several gases into a layer retained by the Earth's gravity between the magnetosphere and the surface of the Earth. The main constituents of the atmospheric gases are nitrogen (N_2) and oxygen (O_2). The combined proportion of these dominant gases is almost 99% in both mass and volume (Saha, 2008, p. 10). Other gases existing in the Earth's atmosphere in less proportions are; carbon dioxide (CO_2), ozone (O_3), argon (Ar) and water (H_2O) in the form of vapour. The distribution of atmospheric gases changes with altitude. Lighter gases are found at high altitudes as they are less affected by gravity than heavier gases that dominate at lower altitudes. The atmosphere is constantly bombarded by solar radiation that span the entire electromagnetic spectrum including infra-red, visible and ultraviolet wavelengths. Some radiation is scattered or reflected back to space by the geomagnetic field, atmospheric gases, clouds or the Earth's surface; some get absorbed by the atmospheric gases leading to parts of the atmospheric being heated and some reach the Earth's surface and heat it. Therefore chemical composition and temperature of the atmosphere are mainly used to divide the atmosphere into different layers.

The terrestrial atmospheric pressure at any layer is proportional to the mass of the air above that layer (Andrews, 2010, p. 10). The atmospheric pressure p, density ρ and temperature T, at any height h are related by

$$p(h) = p_0 \exp\left(-\int_{h_0}^{h} \frac{dh}{H}\right) \tag{1.1}$$

$$\rho(h) = \rho_0 T_0 \exp\left(-\int_{h_0}^{h} \frac{dh}{H}\right) \tag{1.2}$$

where, p_0, ρ_0 and T_0 are the values of p, ρ and T at the reference height h_0 and,

$$H = \frac{kT}{mg} \tag{1.3}$$

is known as the scale height of the neutral atmosphere (Beer, 1974), $k = 1.38 \times 10^{-23}$ J/K is the Boltzmann's constant, m is the mean molecular mass in kg and g is acceleration due to gravity. The pressure p and density ρ generally decrease with increasing height h.

The temperature increases asymptotically above 120 km (see Fig. 1.1b) to a value T_∞ known as the exothermic temperature. The temperature, T, at any height, h, can be approximated by the following equation:

$$T(h) = T_\infty - (T_\infty - T_{120}) \exp\left[-s\,(h - 120)\right] \tag{1.4}$$

where T_{120} is the temperature at 120 km and s is the parameter depending on T_∞, (Davies, 1989, p. 59).

Figure 1.1(a) illustrates a vertically stratified, temperature varying terrestrial atmosphere with four principal layers which are: troposphere, stratosphere, mesosphere and thermosphere. The layer from the ground up to approximately 15 km altitude, in which the temperature decreases with height, is called the troposphere. This layer is bounded from above by a tropopause, and is also referred to as the lower atmosphere. This is the region where weather phenomena such as rain, snow, dust storms, hurricanes, typhoons, tornadoes, thunder and lightning occur (Andrews, 2010, p. 10). The stratosphere is the layer from the tropopause to approximately 50 km altitude. This layer has a positive temperature gradient and is encompassed from above by the stratopause. The layer from the stratopause to approximately 90 km altitude, where the temperature falls again with altitude, is called the mesosphere. This layer is bordered from above by the mesopause. Thin clouds that reflect twilight long after sunset or before sunrise are sometimes observed in the mesosphere proving the presence of water vapour at these heights (Saha, 2008, p. 102) . The middle atmosphere refers to the stratosphere together with the mesosphere. Above the mesopause is the thermosphere, in which the temperature again rises with altitude. This region forms part of the upper atmosphere. The ionosphere, an ionized layer of the atmosphere, is located between the mesosphere and the thermosphere.

1.2.2 Introduction of the ionosphere

The ionosphere is defined as a thick shell of electrons entrenched in the Earth's neutral atmosphere which cloaks the Earth at altitudes between approximately 50 and 1000 km (Mc-

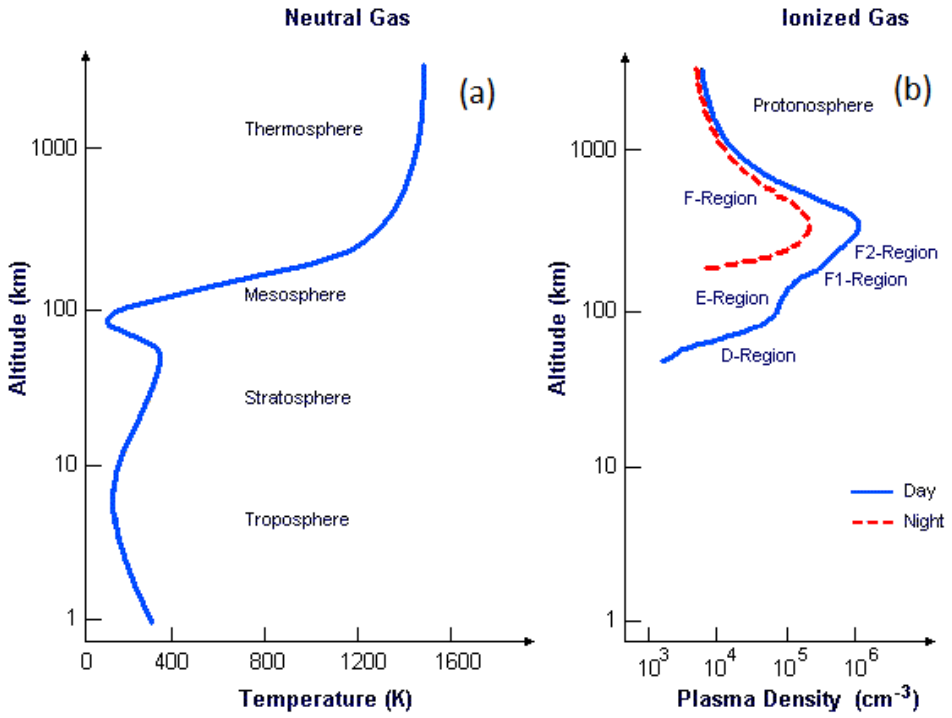

Figure 1.1: The structure of the atmosphere: (a) temperature profile of the stratified atmosphere as a function of altitude and (b) plasma density profile calculated as the number of free electrons per cubic centimeter with the increase in altitude. Source: `http://www.astrosurf.com/luxorion/qsl-hf-tutorial-nm7m3.htm`

Namara, 1991, p. 17). The dynamics of this region are largely controlled by two processes; photoionization and recombination. Photoionization is a process whereby energetic photons from the Sun collide with outer shell electrons of air atoms or molecules with sufficient energy, stripping them off and creating a sea of electrons in the neutral atmosphere. The free electrons in the ionosphere vibrate around the ions in a simple harmonic motion causing the plasma to oscillate with an angular frequency ω, given by

$$\omega_p^2 = \frac{n_e e^2}{m_e \varepsilon_0} \tag{1.5}$$

where n_e is the electron density, $e = 1.602 \times 10^{-19}$ C is the charge of an electron, $m_e = 9.11 \times 10^{-31}$ kg is the mass of an electron and $\varepsilon_0 = 8.85 \times 10^{-12}$ Fm^{-1} is the permittivity of free space. Equation (1.5) can be written in-terms of frequency (measured in Hz) as

$$f_p^2 = 80.5\, n_e \tag{1.6}$$

by evaluating all the constants and recognizing that $f = 2\pi/\omega$. Equation (1.6) allows us to determine the critical frequency of the ionosphere, f_c, that can be used to get the highest frequency needed for the total reflection of a radio wave. This critical frequency (in MHz) is related to the maximum electron density, N_m (in electrons per m^3) by:

$$f_c = 9 \times 10^{-6} N_m^{1/2} \tag{1.7}$$

Recombination is a loss process whereby the electrons combine with positively charged ions to create neutral atoms or molecules. The rate of change of electron concentration with time is expressed by a continuity equation:

$$\frac{\partial n_e}{\partial t} = q - l\,(n_e) - \nabla \cdot (n_e \mathbf{V}) \tag{1.8}$$

where q is the production rate term dependent on radiation intensity and cross section for absorption in the gas, l is the loss term associated with electron loss due to recombination and the divergence term, $\nabla.(n_e\mathbf{V})$, is associated with transport processes resulting in a net drifting velocity $\mathbf{V}$. The dominant source of production is the short wavelength end of the solar emission spectrum, i.e. ultraviolet and less energetic X rays, and the main loss process

is recombination. Extra ionization is caused by solar flares, cosmic rays and the bombardment of particles associated with geomagnetic storms and auroras (Campbell, 1997). The lower parts of the ionosphere are dominated by an electron loss process called attachment, in which the electrons get attached to neutral atoms, thus making them negatively charged ions (McNamara, 1991, p. 17).

Ionospheric plasma density, specifically electron density, varies quite considerable from day to night and with season, geographic or geomagnetic location, solar activity and altitude.

1.2.2.1 Altitude and diurnal variations

Due to the decrease in atmospheric density with altitude the solar radiation encounters fewer electrons to ionize at high altitudes where the atmosphere is very thin. Very little radiation penetrates deep into low altitudes because of the densely populated air region and most of the radiation gets absorbed at higher altitudes. The main factors contributing to the vertical (height) shape of the ionosphere are an increase in radiation with height and as well as a decrease in air density with height.

The amount of ionization of the Earth's atmosphere depends solely on the amount and intensity of radiation it receives. During the day the critical frequencies of the ionospheric layers depend predominantly on the Sun's zenith angle (McNamara, 1991, p. 22). Around noon, when the Sun is at its highest point in the sky (solar zenith = 0), the peak electron density of each layer is at its maximum. During sunset the amount of radiation responsible for the ionized plasma decreases considerably and the recombination processes dominate, therefore depleting the ionosphere. The night time thinning of the ionosphere is mainly caused by rapid collisional recombination at the lower levels after sunset (Campbell, 1997).

Figure 1.1(b), illustrates a typical height and diurnal variation of ionospheric plasma density. The altitude stratification and diurnal variation of the ionosphere are as follows:

a) D region

The *D* region is situated between approximately 50 and 90 km above the surface of the Earth (see Fig 1.1(a)). Electron density in the *D* region as a rule does not have a distinct peak.

This almost isothermal region is densely populated with heavy air molecules and dominated by negative ions, such as O_3^- and NO_2^-, with very low electron densities as a result of lower solar radiation intensities at these heights (Rishbeth and Garriott, 1969, p. 112). Ionization here is mainly due to the Lyman series-α and X-rays with wavelengths less than 10 Å (Banks and Kockarts, 1973, p. 13). Generally the D region is only observed during the day. Since this region is also affected by galactic cosmic rays, the residual amount of ionization by these highly energetic particles sometimes causes radio reflections during the night-time, however, HF radio waves do not get reflected in this region. They tend to get absorbed and lose some of the energy due to the high gas density and high electron collision frequency when passing through to the strongly reflecting F layer above. The D region is a highly turbulent region that is greatly affected by internal gravity waves (Beer, 1974).

b) E region

The E region is located just above the D region from approximately 90 to 150 km altitude. Ionization in this region is caused by extreme ultraviolet rays (EUV), Lyman series-β and the X-rays, wavelengths 10-170 Å (Banks and Kockarts, 1973, p. 13). This is a relatively well behaved ionospheric layer compared to the D region with its properties easily explained by Chapman's theory of ionization of the atmosphere (Rishbeth and Garriott, 1969, p. 92). This layer is also referred to as a dynamo region as it exhibits a dynamo effect caused by the motion of conducting air across the geomagnetic field which induces currents (Beer, 1974; Saha, 2008, p. 74). Thin sporadic clouds of intense iononization, named Sporadic E, often appear in the E-layer. Sporadic E, denoted as (Es), can be extremely thin and dense layers with high levels of iononization. During an Es event, the E region can reflect waves of frequencies up to about 100 MHz which would have otherwise gone further up to the F region (Davies, 1989; McNamara, 1991, p. 97). The peak electron density of the E region is denoted by N_mE and is related to its critical frequency, f_oE, by Equation (1.7). The values of these parameters are highest at noon when the Sun is directly overhead and maximum radiation reaches these altitudes. During the night photoionization ceases, recombination processes dominate and hence result in a weakening of the E region (Hunsucker and Hargreaves, 2002).

c) F region

This is the region of the ionosphere which lies between approximately 150 and 400 km above the Earth's surface dominated by atoms such as O, N_2 and O_2. Extreme ultraviolet radiation (wavelengths between 170 and 911 Å) are responsible for the ionization of this layer of the ionosphere and they produce atomic ions such as O^+, N_2^+ and O_2^+. At night the production of O^+ by photoionization ceases and the transition between atomic and molecular ions, via charge exchange or ion-atom interchange, becomes higher than during the day (Rishbeth and Garriott, 1969, p. 119). The dominant electron loss process in the F region is dissociative recombination. The recombination process in this region occurs in two stages; first ions undergo an ion-atom interchange reaction to form molecular ions, secondly these combine with free electrons via dissociative recombination to form molecules (Rishbeth and Garriott, 1969, p. 113). This F region is the primary region that is used for HF radio communication over long distances as it has the highest electron density and does not disappear. This region usually splits into $F1$ and $F2$ components during the day (Fig. 1.1(b)). The critical frequency of the $F1$ and $F2$ layer are denoted by f_oF1 and f_oF2 respectively and these are related to maximum electron densities N_mF1 and N_mF2 by Equation (1.7). The $F1$ layer becomes more prominent around noon when the solar zenith is zero and completely vanishes during the night. The $F2$ region, however, tends to persist, though at reduced intensity, reaching its minimum just before dawn (Campbell, 1997; Hunsucker and Hargreaves, 2002). At high latitudes, the $E \times B$ convection of ionization from lower daylit latitudes towards the night-side is responsible for the maintenance of the F_2 layer during the long winter nights (Davies, 1989, p. 125).

d) Topside ionosphere

This is the top most region of the ionosphere which extends from $F2$ peak to approximately 1000 km altitude. At these heights geomagnetic fields play an important role and hence, the structure of the topside ionosphere is determined by transport processes (Rishbeth and Garriott, 1969, p. 186). The vertical distribution of electron density at these heights cannot be described simply in terms of the balance between ionization and recombination but rather as the effect of diffusion (Banks and Kockarts, 1973, p. 13). The main gases in this region are the lightest atmospheric components, namely hydrogen (H) and helium (He).

1.2.2.2 Variation with season

The angle at which the Sun's radiation strikes the Earth's surface varies seasonally. In general, the solar ionization flux is greatest in summer when the Earth's summer hemisphere is tilted towards the Sun and lowest in winter when the Earth's winter hemisphere is tilted away from the Sun, and this corresponds to the largest critical frequencies of the D, E and $F1$ regions during the summer. At mid-latitudes, the $F1$ component is frequently observed more on summer days than during winter (Rishbeth and Garriott, 1969, p. 116). The daytime critical frequency $foF2$ is largest during winter than during summer. This is caused by a higher ion loss rate due to seasonal changes in the molecular-to-atomic ratio of the neutral atmosphere (Davies, 1989, p. 126). This phenomenon is known as the mid-latitude seasonal or winter anomaly. The frequency of occurrence of this seasonal anomaly increases with the increase in solar activity (Rishbeth and Garriott, 1969, p. 179).

1.2.2.3 Variation with Solar activity

The Sun's activity is proportional to the number of small dark patches called sunspots seen on the Sun's photosphere. The temperature at the center of the sunspot is about 2000 K lower than the surrounding gas region in the photosphere, explaining the dark appearance (Lang, 2001, p. 95). The sunspot index used to measure the general level of solar activity is given by the Wolf sunspot number

$$R = k\,(10g + s) \tag{1.9}$$

where, k is the observatory factor, g is the number of sunspot groups counted and s is the number of individual sunspots counted. The number of sunspots varies from approximately 0 (least active Sun) to approximately 100 (most active Sun) around every 11 years, this is known as the sunspot cycle. The sunspot cycle is approximately 11 years with a solar maximum period as well as a solar minimum period. The solar cycle is a 22 year cycle which consists of 2 sunspot cycles each with a different solar magnetic orientation. An increase in solar activity leads to more ionization of the atmosphere which then leads to higher critical frequency values of the layers of the ionosphere. The frequency and intensity of geomagnetic storms also vary with solar activity cycle.

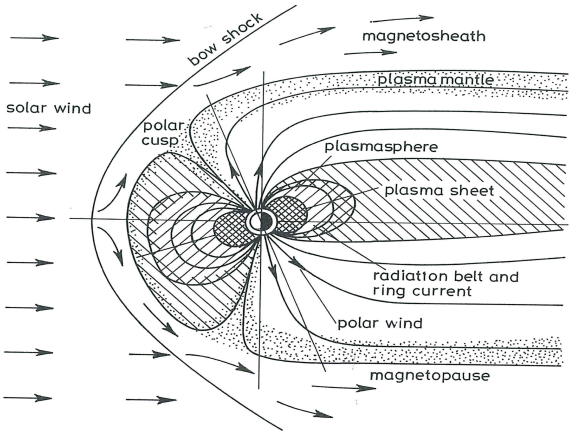

Figure 1.2: Illustration of the Earth's magnetosphere. Adopted from Davies (1989, p. 47)

1.2.2.4 Variation with geographic or geomagnetic location

The Earth's magnetic field owes its existence to the motion of the liquid outer core currents due to the Earth's rotation generated by gravitational processes that formed the Earth's itself (Campbell, 1997). These magnetic field lines form a region around the Earth's atmosphere, called the magnetosphere (see Figure 1.2), that shields life on Earth from the lethal solar and extragalactic radiation. In general, the Earth behaves like a giant dipole magnet with its dipole axis inclined at approximately 11.5° to the axis of rotation (Davies, 1989, p. 39). The magnetic field lines emerge vertically from the magnetic north (borel), run horizontally and parallel at low latitudes, and run down vertically into the magnetic south (austral). The austral is pointed towards the geographic north pole while the borel points towards the geographic south pole. The vector components of the Earth's magnetic field can be represented in two ways (illustrated in Figure 1.3); either by X, Y and Z (XYZ-component) or by H (horizontal), D (declination) and Z (into the Earth) (HDZ-component) (Campbell, 1997). Using simple geometry, the vector components can be related by the following

$$X = H\cos(D), \quad Y = H\sin(D), \quad Z = H\tan(I) \tag{1.10}$$

where I is the inclination angle between the total field $\mathbf{F}$ and the horizontal plain. The total

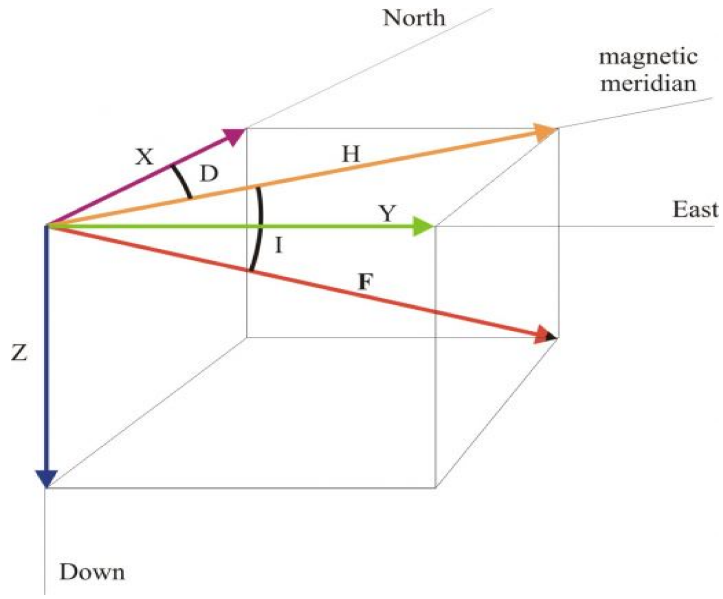

Figure 1.3: Components of the Earth's magnetic field. Source: `http://roma2.rm.ingv.it/en/research_areas/1/earth-s_magnetic_field/8/elements_of_the_geomagnetic_field`.

field strength F is given by

$$F = \sqrt{X^2 + Y^2 + Z^2} = \sqrt{H^2 + Z^2} \tag{1.11}$$

Ionospheric response to magnetic storms

Solar winds are supersonic (speeds of approximately 400-1000 ms^{-1}) plasma waves ejected from the Sun's corona (Davies, 1989; Saha, 2008). The Earth's magnetic field is constantly being disturbed by the solar processes such as solar winds and their frozen-in interplanetary magnetic fields (IMF) that deposit huge amounts of energetic charged particles onto the magnetosphere, causing geomagnetic storms (Campbell, 2001, p. 44). When the solar wind couples with the magnetosphere, a bow shock that compresses the magnetic field is created. During this coupling some of the charged particles in the solar wind get trapped by the Earth's magnetic field while the rest move along the stretched night side, which is the tail of the magnetosphere. The accumulation of these charged particles at the magneto-tail leads to instability in the magnetosphere, resulting in magnetospheric substorms. Magnetospheric substorms, sometimes referred to as auroral substorms, are disturbances in the Earth's magnetosphere that cause the energy accumulated by the charged particles at the magneto-tail to

be released from the tail of the magnetosphere and injected into the high latitude ionosphere, that last for up to several hours (Davis and Sugiura, 1966; Rostoker et al., 1980). Solar particles trapped by the field lines spiral around the field lines between the two poles and also drift around the Earth's magnetosphere, causing ring currents (Davies, 1989, p. 49).

The ionosphere over middle latitude regions (in the geographic latitude range of about 23° - 66°) is relatively less dynamic when compared to low (from 0° to approximately 23° latitudes) and high (latitudes $\gtrapprox 66^\circ$) latitudes. Some of the challenges at high latitudes arise because the Earth's magnetic field is almost vertical at the geomagnetic poles. These almost vertical field gradients allow particles from the Sun to spiral around the field line and penetrate deeper into the low levels of the atmosphere. These particles then collide with the atoms and molecules of the neutral atmosphere causing increased ionization in a process named collisional ionization (McNamara, 1991, p. 98). Collisional ionization at high latitudes escalates the electron density of the ionosphere influencing HF communication. The visual effects of collisional ionization can be seen over high latitudes in the form of auroras.

The ionosphere over low latitudes is characterized by the fountain effect which redistributes plasma from the geomagnetic equator to low latitudes. This combined effect of the east-west electric field and the north-south horizontal magnetic field ($E \times B$), results in electrons drifting upward (Davies, 1989; McNamara, 1991, p. 30). Rapid increases in critical frequencies during sunrise at low latitudes make it difficult to predict and observe HF efficiently (McNamara, 1991, p. 97).

1.2.3 Atmospheric gravity waves

Atmospheric gravity waves (AGW) are defined to be the up and down movement of the air parcels away from the source, by the uplifting force due to buoyancy, sometimes referred to as buoyancy waves. The AGWs observed in the thermosphere and ionosphere can have numerous local or remote sources such as solar terminator, solar eclipse, auroral activity, wind shear, large convective systems and tropospheric weather (Vadas and Fritts, 2006; Fritts and Alexander, 2003; MacDougall and Jayachandran, 2011). A solar terminator is a moving circular line, approximately the diameter of the Earth, that separates the day-side from the night-side. The terminator marks an important transition from the daytime to the nighttime ionosphere. It represents a region of sharp change in the energy input from the solar radiation, which consequently leads to strong gradients in the Earth's atmospheric and ionospheric

parameters such as density, temperature and pressure. Sharp gradients create instability in the ionosphere which give rise to the ionospheric irregularities and non-uniformity (Somsikov, 1995; Liu et al., 2009). Song et al. (2013) suggested that the heating and cooling effects associated with the terminator in the transition region, between F1 and F2 layers (approximately 150 - 250 km altitudes), could generate AGW. Using a HF radar to study AGW, Bristow et al. (1994) concluded that the auroral electroject current can excite AGWs either by direct momentum transfer from ions to the neutral gas, via the Lorentz force, or by heating of the neutral gas, via Joule heating. An AGW packet is both anisotropic and dispersive. Its anisotropic nature leads to waves propagating differently in different directions and its dispersive nature leads to different wave velocities at different wavelengths (McNamara, 1991, p. 37).

Hunsucker (1982) noted that AGW excited by lower atmospheric processes tend to propagate more freely whereas gravity waves excited by high latitude processes appear ducted. These waves are known for their efficient coupling of energy and momentum from their source regions, usually from the lower atmosphere to the middle and upper atmosphere (Vincent, 2009). Convective instabilities in the troposphere can lead to upward drifting of moist air within the convective plumes. If strong enough, these convective plumes can drift up into the stratosphere and trigger AGW (Alexander, 1995; Lane et al., 2001). Neutral winds tend to create channels of clear propagation of AGW from the ground to the thermosphere (Cowling et al., 1971). These winds also influence the observations of AGWs and TIDs at ionospheric heights. Wind filtering processes play a very important role in AGW propagation into thermospheric heights. Only gravity waves propagating against the background wind move into higher altitudes (Cowling et al., 1971; Waldock and Jones, 1984). Hines (1991) observed that AGWs propagate primarily upward and tend to grow in amplitude with an increase in height in response to the depleting atmospheric density. Small amplitude gravity waves can propagate upwards, growing in size as a result of decrease in air density with altitude, into the thermosphere before dissipating (Francis, 1973; Vadas, 2005; Vadas and Liu, 2009). Dissipation of gravity waves trigger background wind shears horizontally in the direction the wave was propagating, producing secondary gravity waves (Fritts and Alexander, 2003). A number of studies have associated LSTIDs with secondary AGW generated from thermospheric body forces. These body forces are said to be created from the dissipation of primary AGW via deep tropospheric convention (e.g. Vadas and Crowley, 2010; Zhou et al., 2012). AGWs cause perturbations in the neutral and ionized atmospheric parameters such as; density, temperature and wind velocity.

Fritts and Alexander (2003) showed that the gravity wave equation can be written in the form

$$\hat{\omega} = \frac{N^2\left(k^2+l^2\right)+f^2\left(m^2+\frac{1}{4H^2}\right)}{k^2+l^2+m^2+\frac{1}{4H^2}} \tag{1.12}$$

or in terms of vertical wavenumber m, as

$$m^2 = \frac{\left(k^2+l^2\right)\left(N^2-\hat{\omega}^2\right)}{\left(\hat{\omega}^2-f^2\right)} - \frac{1}{4H^2} \tag{1.13}$$

This equation describes the dispersion relation of AGW which relates the wave's angular frequency $\hat{\omega}$ to the wavenumbers (k, l, m) and the local Brunt-Väisälä (or buoyancy) frequency N. AGW excited by convective plumes and clusters are high frequency waves (Vadas and Crowley, 2010) ($\hat{\omega} \gg f$ hence, the Coriolis term can be omitted and setting $m^2 \gg 1/4H^2$) described by Boussinesq dispersion:

$$\hat{\omega} = \frac{N^2\left(k^2+l^2\right)}{k^2+l^2+m^2} \tag{1.14}$$

and the wavelength λ of the AGW is given by

$$\lambda = 2\pi(k^2+l^2+m^2)^{-1/2} \tag{1.15}$$

The gravity wave's intrinsic frequency can be linked to its observed frequency, $\omega = 2\pi/\tau$ (where τ is the period of the AGW), through

$$\hat{\omega} = \omega + k_H U_H \tag{1.16}$$

where $k_H = 2\pi/\lambda_H$ is the wavenumber in the horizontal and

$$U_H = \frac{(k\bar{u}+l\bar{v})}{k_H} \tag{1.17}$$

is the background, neutral wind velocity in the direction of AGW propagation.

1.2.3.1 Travelling ionospheric disturbances

Travelling ionospheric disturbances (TIDs) are quasi-periodic perturbations observed in an electron dense plasma produced by AGWs via the energy and momentum coupling between the neutral air and the ionized plasma (Hunsucker, 1982; Hines, 1991). Afraimovich et al. (2003) considered TIDs as essentially a net interference wave field of AGWs of different origins and their interaction with the ionospheric plasma. TIDs have been measured by a number of instruments including ionosondes, Super Dual Auroral Radar Network (SuperDARN) and incoherent radars, GPS satellites, and HF Doppler systems (for e.g. Waldock and Jones, 1986; Galushko and Paznukhov, 1998; Afraimovich et al., 1998; Hajkowicz, 1990; He and Dyson, 2002). The waves are smaller in amplitude and period when compared to most ionospheric disturbances and have been observed to traverse horizontal distances of up to 3000 km. TIDs are usually categorized into two distinct types, the large scale travelling ionospheric disturbances (LSTIDs) which are associated with geomagnetic activity, and the medium scale travelling ionospheric disturbances (MSTIDs) associated with a variety of atmospheric sources and their occurrence commonly.

Vadas (2007) theorized that in the thermosphere (at heights $> 180\,\text{km}$) convectively generated gravity waves dissipate and are likely to generate MSTIDs and LSTIDs which can be observed during geomagnetically active and quiet conditions.

LSTIDs

In general, LSTIDs are listed as having horizontal phase speeds from approximately 400 to more than 1000 m/s (comparable with the acoustic speed in the thermosphere), horizontal wavelengths greater than 1000 km and periods in the range of about 30 minutes to 3 hours (Francis, 1973; Hunsucker, 1982; Waldock and Jones, 1984, 1986, 1987; Afraimovich et al., 2003; Crowley and Rodrigues, 2012; Zhou et al., 2012). LSTIDs are thought to be excited in the auroral regions by processes such as auroral electrojets, sudden intense particle precipitation and auroral electrojet peaks (Georges, 1968; Hunsucker, 1982). Momentum transfer, via Lorentz force, and heating, via Joule heating and particle precipitation, are the two mechanisms by which LSTIDs are generated (Francis, 1975; Hunsucker, 1982). LSTIDs usually propagate meridionally from the polar regions towards the equator (Valladares and Hei, 2012). Although they are characterized by long horizontal wavelengths and high veloc-

ities, and thus traverse long distances, they are only occasionally observed in the equatorial regions (MacDougall et al., 2009).

Various authors have previously associated LSTIDs with geomagnetic storm activity (e.g. Ding et al., 2007; Perevalova et al., 2008; Amabayo et al., 2012). Some authors have also associated them with auroral events and substorms (e.g. Davis and da Rosa, 1969; Davis, 1971; Hajkowicz, 1990; Bristow et al., 1994). However other studies, such as Vadas and Crowley, 2010; Zhou et al., 2012, have also illustrated that LSTIDs can be excited by secondary AGWs generated from thermospheric body forces created from the dissipation of the primary AGWs via deep tropospheric convection.

MSTIDs

MSTIDs are characterized by periods less than an hour, horizontal velocities less than the acoustic speed and wavelengths that are few hundreds of kilometers (Hunsucker, 1982; Waldock and Jones, 1984, 1986, 1987; Afraimovich et al., 2003; Otsuka, 2004; Hernández-Pajares et al., 2006; Kutiev et al., 2009; MacDougall and Jayachandran, 2011; Hernández-Pajares et al., 2012). MSTIDs are said to be originating primarily from tropospheric weather and mountain turbulence (Valladares and Hei, 2012). Beer (1974) suggested that MSTIDs show a tendency to approach from any general direction. MSTIDs tend to disappear or lose their shape within 2000 km from the source, meaning that MSTIDs generated by AGW from the troposphere cannot be observed more than 2000 km away from where they were excited (Beer, 1974; Vadas, 2007). Vadas (2007) also demonstrated that some MSTIDs could be directly associated to thermospheric convection. Some studies linked MSTIDs with solar terminator occurrences (e.g Hernández-Pajares et al., 2006; MacDougall and Jayachandran, 2011; Sindelarova et al., 2012; Chum et al., 2012). MSTIDs are observed more frequently, compared to LSTIDs, and thus have been studied extensively especially in the middle and high latitude regions (e.g. Hunsucker, 1982; Waldock and Jones, 1984, 1986, 1987; Hines, 1991; Bristow et al., 1994; Bristow and Greenwald, 1996).

1.2.4 Solar terminator

A solar terminator is a moving circular line, approximately the diameter of the Earth, that separates the day-side from the night-side. The terminator marks an important transition from

the daytime to the nighttime ionosphere. It represents a region of sharp change in the energy input from the solar radiation, which consequently leads to strong gradients in the Earth's atmospheric and ionospheric parameters such as density, temperature and pressure. Sharp gradients create instability in the ionosphere which give rise to the ionospheric irregularities and non-uniformity (Somsikov, 1995; Liu et al., 2009). Song et al. (2013) suggested that the heating and cooling effects associated with the terminator in the transition region, between F1 and F2 layers (approximately 150 - 250 km altitudes), could generate AGW. While studying the sources of TIDs over mid-latitude *F* region, MacDougall and Jayachandran (2011) also concluded that solar terminators were responsible for some of the observed TIDs. Recent studies have successfully linked TIDs to solar terminators (for e.g. Galushko and Paznukhov, 1998; Afraimovich and Voyeikov, 2009; Afraimovich et al., 2010; MacDougall and Jayachandran, 2011).

1.3 Thesis Overview

The following chapters of this thesis include the following information:

Chapter 2 discusses the instruments and model(s) used to acquire data that were used in the study:

- The theory of HF radio propagation.
- The description of the HF Doppler radar, the Doppler radar network, data logging and storage.
- An introduction to GPS satellites, the magnetometer and data acquisition.
- The horizontal wind model (HWM07) used to model the ionospheric wind at thermospheric heights.

Chapter 3 introduces:

- The techniques and tools employed and developed for processing the collected data while detailing exactly how they were used.

- The tools and digital signal processing techniques that were used for processing data.

Chapter 4 discusses:

- The results of the analyzed data obtained by methods described in chapter 2 and processes using techniques mentioned in chapter 3.
- Statistical information about the horizontal propagation characteristics of the observed TIDs such as velocities and direction of propagation as well as TIDs' period and wavelengths.
- The probable sources of the observed TIDs.

Chapter 5 summarizes and concludes:

- The findings of the research while revisiting the goals stated above and reflecting upon the research undertaken.

Chapter 2

Data Sources and Instrumentation

This chapter includes information on the datasets used as the basis for the analysis discussed in Chapter 3. During the course of this research project a number of different datasets were used. The primary source of data was the HF Doppler receiver located in Hermanus ($34°25'30''S,\ 19°13'30''E$) which recorded Doppler frequencies from three HF transmitters, each located roughly 100 km from the receiver. Digisonde DPS 4D, which is located at the same place as the receiver of the Doppler sounding system was used to determinate the reflection height of the signal. Other dataset sources used include: the Fluxgate 3-axis magnetometer also located in Hermanus, used to measure the Earth's magnetic field variations; GPS satellite data obtained from TrigNet[1], used to calculate the total electron content (TEC); and the HWM07 model from the National Space Science Data Center[2] which modelled the thermospheric winds at the Doppler signal's reflection height.

2.1 HF Doppler radar

2.1.1 HF propagation

HF radio communication is a way of exchanging information wirelessly by making use of the electromagnetic waves in the radio (frequencies 3 - 30 MHz) spectrum. The basic system

[1] `http://www.trignet.co.za/`

[2] `http://nssdcftp.gsfc.nasa.gov/models/atmospheric/hwm07/`

for HF radio communication is comprised of: the transmitter responsible for modulating and sourcing out the message in the form of electrical energy; the antenna used for converting electrical energy into electromagnetic waves; propagation medium such as the air molecules that allow the radio wave to pass from molecule to molecule via the energy transfer between outer electrons of adjacent molecules; and the receiver that captures, amplifies and demodulates some of the energy of the electromagnetic wave so as to interpret the message. The ionosphere is an electrically dense medium that naturally reflects HF radio waves which can be used to achieve radio communication over large distances. The dynamic nature of the ionosphere, such as the movement of TIDs, influences changes, both with space and time, on HF radio wave parameters such as phase, amplitude, angle of arrival, frequency and polarization. Observations made of these parameters at a number of spaced stations on the ground allow for the measurement of the speed and direction of travel of these ionospheric disturbances. This is known as ionospheric sounding (McNamara, 1991, p. 35).

A HF Doppler radar is one of the ionospheric sounders that makes use of this technique to measure the speed and direction of travel of the TIDs. Illustrated in Figure 2.1 is an example of the propagation mode of an ionospheric reflected sky wave signal that is used in HF Doppler sounding. An HF radio signal is transmitted at some elevation angle E, gets reflected at point P in the ionosphere and is registered by receiver R. The angle made by transmitted signal with the normal at point P is called the angle of incidence. The HF Doppler sounding technique has been studied and used extensively to probe the ionosphere (refer to Georges, 1968; Vincent and Reid, 1983; Crowley et al., 1984; Waldock and Jones, 1986; Cheng et al., 1997; Hunsucker and Hargreaves, 2002; He and Dyson, 2002; Chum et al., 2008; MacDougall et al., 2009; Petrova et al., 2009; Chum et al., 2010).

If a dimensionless reduced height,

$$z = \int_{h_0}^{h} \frac{dh}{H} \tag{2.1}$$

then for an isothermal atmosphere Equation (2.1) becomes

$$z = \frac{h - h_0}{H} \tag{2.2}$$

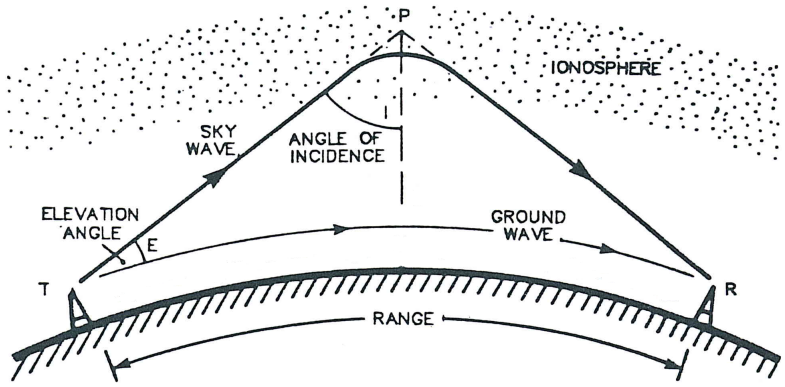

Figure 2.1: HF radio sky wave sent from a transmitter T, reflected through the ionosphere and picked up by the receiver R. Adopted from McNamara (1991, p. 39).

For a HF signal transmitted at an angle E from the ground (refer to Figure 2.1) to be reflected, it must obey the refraction law given by

$$\mu(z)\,sin\,\alpha = \mu_0\,sin\,\alpha_0 \tag{2.3}$$

where α is the angle between the wave normal and the perpendicular to the surface of constant refractive index, and μ_0 is the value of the refractive index at the base of the reflecting layer. Here, μ is the refractive index for an electromagnetic wave propagating through cold magnetized collisionless plasma described by the Appleton-Hartree formula as:

$$\mu^2 = 1 - \frac{2X\,(1-X)}{2\,(1-X) - Y_T^2 \pm \left[Y_T^4 + 4\,(1-X)^2\,Y_L^2\right]^{1/2}} \tag{2.4}$$

where, in this chapter $X = \omega_p^2/\omega_r^2 = Ne^2/\varepsilon_0 m_e \omega_r^2$ is the electron plasma frequency term, $Y_L = \omega_{ceL}/\omega_r = eB_L/m_e\omega_r$ is the longitudinal electron gyro frequency term and $Y_T = \omega_{ceT}/\omega_r = eB_T/m_e\omega_r$ is the transverse electron gyro frequency term with B the ambient homogeneous magnetic field. If the effects of the magnetic field are ignored, Equation (2.4) becomes

$$\mu^2 = 1 - X = 1 - \frac{Ne^2}{\varepsilon_0 m_e \omega_r^2} \tag{2.5}$$

where $f_r = \omega_r/2\pi$ is the operating HF radio wave frequency in Hz. The most usual mechanism for the reflection of a radio signal by the ionosphere, which applies in the HF radio band, is actually a gradual bending of the ray towards the horizontal as the refractive index of the ionospheric medium decreases with altitude (Hunsucker and Hargreaves, 2002). Higher radio frequencies tend to be reflected from greater heights, however, if the frequency is too high (i.e. $f_r > f_c$) there may be insufficient bending and the signal then penetrates the layer and is lost to space. This is the first complication of radio propagation.

2.1.2 HF Doppler sounding

Continuous wave (CW) Doppler sounding is a method of observing ionospheric motion by recording HF radio transmissions reflected from the F region, (refer to Waldock and Jones, 1986; Crowley and Rodrigues, 2012). Transverse motion of the reflection region in the ionosphere induces a change in the radio wave path, hence imposing a Doppler shift on the received signal given by

$$\Delta f = -(f_r/c)\left(\frac{dP}{dt}\right) \tag{2.6}$$

where the signal phase path P is given by

$$P = 2\int_0^h \mu dl \tag{2.7}$$

and, c is the speed of light, and l is the distance from the ground to the height of the reflection layer h. Equation (2.6) can then be written as

$$\Delta f = -2\frac{f_r}{c}\frac{d}{dt}\left(\int_0^h \mu dl\right) = -2\frac{f_r}{c}\int_0^h \frac{\partial \mu}{\partial n_e}\frac{\partial n_e}{\partial t} dl \tag{2.8}$$

The Doppler shift of the received signal is thus measured from variations in the receiver output frequency, which is recorded directly. Using Equation (2.5) to evaluate $\partial\mu/\partial n_e$, and

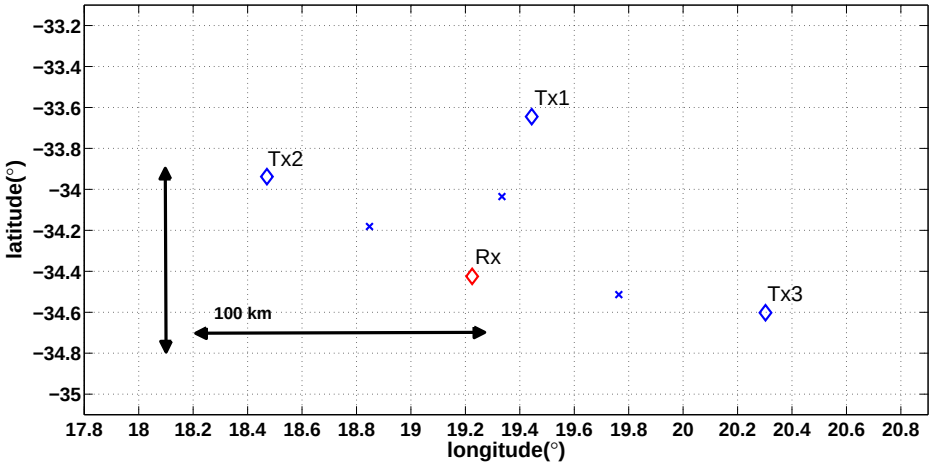

Figure 2.2: Layout of the HF Doppler radar deployment in the Western Cape province: Tx1-Worcerster transmitter, Tx2-Cape Town transmitter, Tx3-Arniston transmitter and Rx1-Hermanus receiver. The crosses indicate the midpoints (approximate signal reflection points) between transmitter and receiver. Each transmitter is about 100 km from the receiver.

substituting the solution into Equation (2.8), Doppler frequency can be given by:

$$\Delta f = \frac{1}{4\pi^2 c\varepsilon_0 m_e f_r} \int_0^h \frac{1}{\mu} \frac{\partial n_e}{\partial t} dl \tag{2.9}$$

Investigating Equation (2.9) closely reveals that, as the signal propagates upwards into the ionosphere, its phase and amplitude are greatly affected by the refractive index term, $1/\mu$, and the electron density profile, $\partial n_e/\partial t$. Waldock and Jones (1986) suggested that by making use of more than three transmitters, or receivers, it is possible to monitor different parts of the ionosphere simultaneously and by using the time delays between the event signatures on the different HF propagation paths, with the knowledge of the reflection points, it is possible to deduce the velocity of the travelling ionospheric irregularities.

Figure 2.2 illustrates a quasi-isosceles geographical configuration of the South African Doppler radar with three CW transmitters Tx1, Tx2 and Tx3 in Worcester, Cape Town and Arniston respectively, and one digital receiver Rx in Hermanus. The system consists of circularly polarized receiving and transmitting antenna sets, and a digital data acquisition system. The radar system, operating at a central frequency of 3.5945 MHz, is driven on a 10 MHz oven controlled crystal oscillator (OCXO) clock integrated using a direct digital synthesizer (DDS)

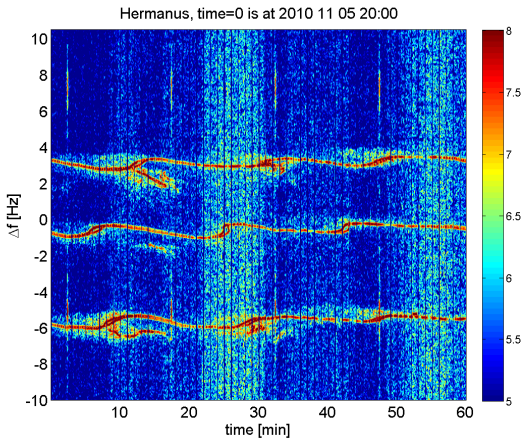

Figure 2.3: Spectrogram with Doppler shifted frequencies from all three transmitting stations.

(Chum et al., 2008, 2012; Sindelarova et al., 2012). The clock is synchronized with GPS to ensure precision. During suitable propagation conditions the transmitted signals are reflected by the ionosphere and are received at the base station simultaneously. To differentiate the incoming signals from each station, the actual transmitted frequency is shifted by 4 Hz from the nominal frequency in each station.

2.1.3 HF Doppler Data acquisition and storage

Radar data are stored in 15 minute binary files. This corresponds to a total of 96 Doppler data files logged each day. At the beginning of each minute in a 15 minute data file is a header of 64 Bytes containing a time stamp and identification string of the receiver. The data sampling frequency is 305.1758 Hz, which actually corresponds to approximately 53.68 s of data being stored, with about 6 s of calling mark transmission. A data block of each minute consists of 16384 samples stored in two channels shifted by 90 degrees in phase, with a 16 bit resolution, giving a total of $4 \times 16384 = 65536$ Bytes of data stored altogether. The data are then visualized by means of spectrograms (refer to Figure 2.3).

The HF Doppler radar used in this study has had frequent interruptions due to technical problems since its installation in May 2010, resulting in intermittent data availability. Figure 2.4 illustrates an inventory of the data for the year 2010, 2011 and 2012. The color intensity represents the amount of data available each day. The colour representation for data availability was as follows: red denoted 'all day' data files available; green for 'partial day' data

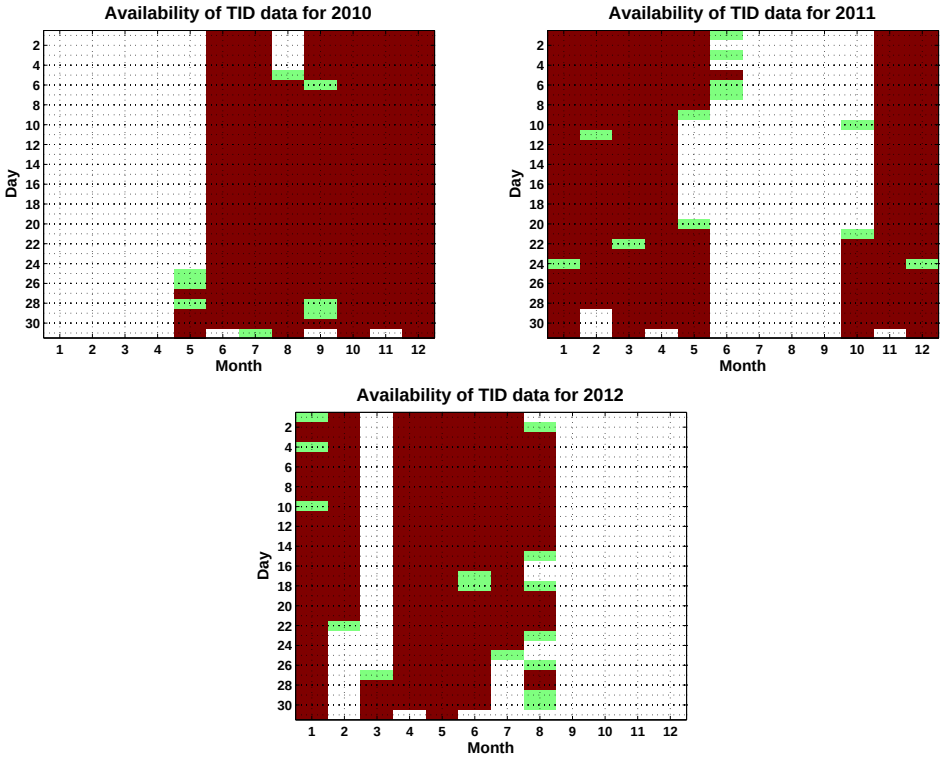

Figure 2.4: HF radar data inventory with the colour intensity representing the Doppler data availability on a particular day. White = no files, Red = all files available and Green = some files missing.

availability; and white for zero data available. There were cases when data was available but unusable, for example noisy (Figure 2.5 left) or blank (Figure 2.5 right).

2.2 GPS satellites

The global positioning system (GPS), is a satellite based navigation system consisting of medium Earth orbit satellites (MEO) that orbit in the region between low Earth orbit (altitude of approximately 2000 km) and the geostationary orbit (altitude of approximately 36000 km), developed by the United States Department of Defense in the 1970s. The system was initially developed for military application and configured to have 24 MEO satellites (refer to Figure 2.6) equally placed in three orbits with inclinations of 63 degrees relative to the equatorial plane (Ta, 2011). To date, GPS forms part of a global navigation satellite system (GNSS) developed by a consortia of countries for military, civil, scientific and commercial interests.

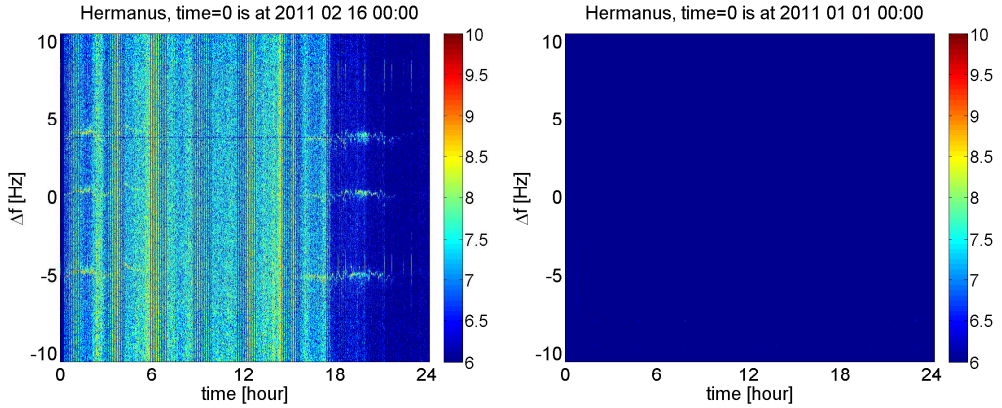

Figure 2.5: Unusable radar data.

There are currently about 30 GPS satellites orbiting the Earth at approximately 20200 km orbital height in six orbiting planes at 55° inclination relative to the equatorial plane with a period of about 12 hours (Misra and Enge, 2006, p. 33). This configuration ensures that a user with a clear view of the sky has at least six satellites within line of sight from almost anywhere on the Earth's surface. The system is capable of providing information, almost instantaneously, about position and time under any weather conditions anywhere on Earth, as long the line of sight to at least four GPS satellites is unobstructed.

The GPS system operates with two continuous radio frequencies in the L-band (1-2 GHz band) labelled, L1: f_{L1} = 1575.42 MHz and L2: f_{L2} = 1227.60 MHz. Dual frequency measurements allow for correction for the ionospheric propagation delay (Misra and Enge, 2006, p. 20). In addition, the system also works with L3: f_{L3} = 1381.05 MHz and L5: f_{L5} = 1176.45 MHz signals which are associated with classified payloads on board the satellites and aeronautical safety of life, respectively (Misra and Enge, 2006; Montenbruck et al., 2012). Another band, L4: f_{L4} = 1379.913 MHz, is being studied for additional ionospheric correction[3]. The pseudorange (apparent distance between a satellite and the GPS receiver) uses two pseudorandom noise (PRN) signals that are embedded on the L1 and L2 carrier signals. The PRN codes modulated onto the carriers prevent the signals from different satellites from interfering with each other as they use the same carrier signals (Hofmann-Wellenhof et al., 1997; Misra and Enge, 2006, p. 16). The L1 signal, designated for the standard positioning services (SPS), is composed of the carrier frequency f_{L1}, the coarse/acquisition code (C/A code) and the precision (encrypted) code (P-code). The L2 signal with a carrier frequency f_{L2} carries a P-code only and is used for military purposes.

[3] http://www.radio-electronics.com/info/satellite/gps/signals.php

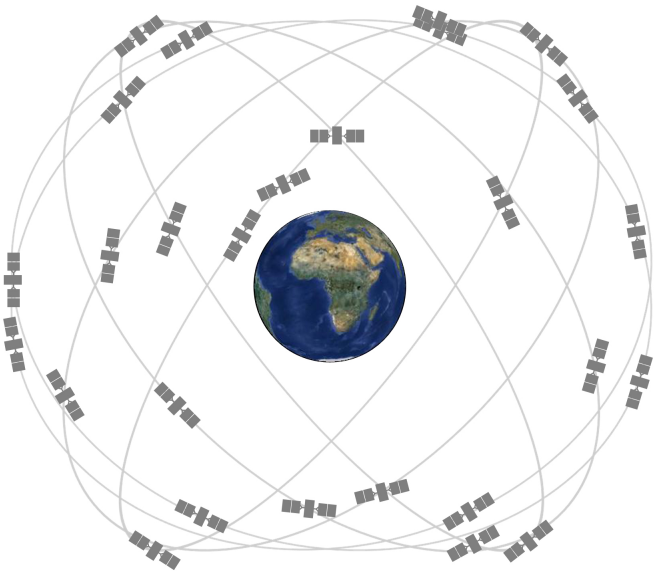

Figure 2.6: MEO GPS satellite constellation adopted from `http://www.gps.gov/systems/gps/space/`.

GPS data are available in either binary or ASCII format regardless of whether they are obtained directly from a receiver or from a storage file. The current standard for storage of raw GPS data is the Receiver Independent Exchange (RINEX) format. This format is designed to evolve over time, adapting to new types of measurements and new satellite navigation systems. The RINEX file generally encompasses a header containing information about the GPS receiver and a block of data containing the observation time, carrier phase measurements and pseudorange measurements.

2.2.1 GPS TEC measurements

GPS signals are negatively affected by the dispersive properties of a medium through which they propagate. The ionosphere and the troposphere greatly influence the propagation of the radio signal from the satellite to the receiver, although the ionosphere is the dominating influence (Hofmann-Wellenhof et al., 1997; Misra and Enge, 2006). The time the signal takes to travel along the path l between the receiver R and the transmitting satellite S is given by:

$$\tau = \frac{1}{c} \int_{S}^{R} \mu(l) dl \tag{2.10}$$

When the GPS signal propagates through the ionosphere, its phase and group propagation properties differ slightly (Misra and Enge, 2006). The phase properties are related to the carrier component of the signal by:

$$v_p = \frac{\omega_c}{k} \tag{2.11}$$

$$\mu_p = 1 - \frac{40.3 n_e}{f^2} \tag{2.12}$$

and the group properties are related to the modulation component given by:

$$v_g = \frac{d\omega}{dk} \tag{2.13}$$

$$\mu_g = 1 + \frac{40.3 n_e}{f^2} \tag{2.14}$$

where k is a wavenumber. The phase and the group refractive indices defined by Equations (2.12) and (2.14) respectively are related by:

$$\mu_g = \mu_p + f\frac{d\mu_p}{df} \tag{2.15}$$

Examining Equations (2.12) and (2.14) closely reveals that the carrier phase μ_p is measured too short and the modulating or code phase $\mu_g$is measured too long, when compared to the signal travelling through non-dispersive medium. This phenomenon is known as the code-carrier divergence (Misra and Enge, 2006, p. 161). The phase and group delay (in meters), I_ϕ and $I_\rho$respectively, of the GPS signal propagating through the ionosphere are given by Equations (2.16) and (2.17),

$$I_\phi = -\frac{40.3 TEC}{f^2} \tag{2.16}$$

$$I_\rho = \frac{40.3 TEC}{f^2} \tag{2.17}$$

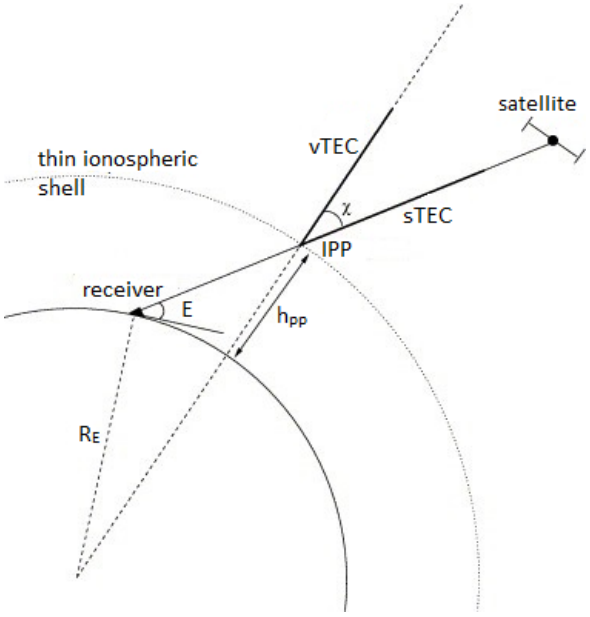

Figure 2.7: The GPS signal propagation path length through the ionosphere. Adopted from the work of Nava et al. (2007).

where the total electron content (TEC) is defined to be the number of free electrons in the plasma that are in the path of the GPS signal, given by the following:

$$TEC = \int_{S}^{R} n_e(l)\, dl \tag{2.18}$$

and is measured in TEC units (TECU), where 1TECU = 10^{16} electrons per m^2. Figure 2.7 illustrates the slant total electron content (sTEC) obtained by integrating the signal from the satellite, which pierces the ionosphere at the ionospheric pierce point (IPP) at some mean ionospheric height h_{PP}, to the ground receiver with an elevation E. The sTEC can be related to the vertical TEC (vTEC) using the following:

$$sTEC = \frac{1}{cos(\chi)}\, vTEC \tag{2.19}$$

where,

$$cos(\chi) = \left[1 - \left(\frac{R_E\, cos E}{R_E + h_{PP}}\right)^2\right]^{-1/2} \tag{2.20}$$

is called the obliquity factor, χ is the satellite zenith angle at the IPP and R_E is the radius of the Earth. For a user with a dual GPS receiver (L1 & L2 signals), the pseudorange measurement expressions can be rewritten to give the estimates for the ionospheric delay at L1 given by

$$I_{L1} = \frac{f_{L2}^2}{\left(f_{L1}^2 - f_{L2}^2\right)} \left(\rho_{L2} - \rho_{L1}\right) \tag{2.21}$$

where ρ_{L1} and ρ_{L2} are pseudorange measurements at L1 and L2, respectively; and the carrier phase measurement can also be rewritten to give estimates of the ionospheric delays given by

$$I_{L1} = \frac{f_{L2}^2}{\left(f_{L1}^2 - f_{L2}^2\right)} \left[\lambda_{L1}\left(\phi_{L1} - N_{L1}\right) - \lambda_{L2}\left(\phi_{L2} - N_{L2}\right)\right] \tag{2.22}$$

where ϕ_L is the carrier phase measurement, λ_L is the carrier wavelength and N_L is the integer ambiguity (Misra and Enge, 2006). Since the carrier phase measurements are less noisy when compared to pseudorange measurements, Equation (2.22) is more accurate but ambiguous in N_L whereas, Equation (2.21) is less accurate but unambiguous (Misra and Enge, 2006, p. 167).

A software developed at the Institute for Scientific Research at Boston College was used to calculate vTEC. This software uses carrier phase and pseudorange measurements for L1 and L2 frequencies to remove error effects such as receiver-satellite distance, clock offsets, and tropospheric delay to calculate sTEC (Sardón and Zarraoa, 1997). The sTEC values are then corrected for frequency-dependent effects such as the differential instrumental biases which are obtained from the University of Bern, and the receiver bias that is calculated by minimising the TEC variability between 02:00 and 06:00 LT (Valladares et al., 2009).

2.3 Fluxgate Magnetometers

Devices for measuring the Earth's magnetic field are called magnetometers. Important classes of magnetometers include using a rotating coil, Hall effect magnetometers, nuclear magnetic resonance (NMR) magnetometers, superconducting quantum interference device (SQUID) magnetometers, and fluxgate magnetometers.

The three-axis fluxgate magnetometer (FGE-MGN) is one of the types of magnetometers in operation at the Hermanus station. This magnetometer was designed and built by the Danish Meteorological Institute[4]. The sensor unit consists of three orthogonally mounted sensors on a marble cube. The marble cube is suspended by two strips of crossed phosphor-bronze working as a Cardan's suspension to compensate for pillar tilting which might cause a base-line drift. Although the three-axis systems have many problems, arising from the cross-field effect, they are very popular because of their simplicity and low price (Ripka, 2003). In order to improve long-term stability these sensors have compensation coils wound on quartz tubes, limiting sensor offset to only a few nT per year. The three-axis sensor configuration makes it possible for the sensor to measure the H, D and Z (i.e. horizontal intensity, declination and vertical intensity respectively) vector components of the Earth's magnetic field simultaneously. These vector components of the field are related to the X, Y and Z (i.e. the north and east components of the horizontal intensity, and the vertical intensity respectively) components by Equation (1.10). In this study, the H-component of the Earth's magnetic field was used to check for correlations between the observed LSTIDs and geomagnetic activity.

Data are sampled every 5 seconds and according to the international real-time magnetic observatory network (INTERMAGNET) specifications a Gaussian filter is applied in order to obtain the final minute data series. Data are then logged into an ASCII file containing a header and column headers. INTERMAGNET[5] is the global network of observatories that monitor the Earth's magnetic field according to strict internationally accepted standards. The Hermanus station is one of four African INTERMAGNET observatories.

2.4 Horizontal Wind Model (HWM07)

HWM07 is a comprehensive empirical global model of horizontal winds in the middle and upper atmosphere. This model is a sequel to the Horizontal model series (HWM87, HWM90, HWM93) (Hedin, 1987; Hedin et al., 1988; Hedin and Biondi, 1991).

Initially, HWM87 used a limited set of vector spherical harmonics to model only the upper thermospheric winds' spatial and temporal variations as it was based on thermospheric data obtained from the Atmospheric Explorer E and Dynamics Explorer 2 satellites[6]. HWM87

[4] http://www.dmi.dk/en/vejr/
[5] http://www.intermagnet.org/
[6] http://www.planet4589.org/space/misc/explorer.html

could only model thermospheric winds at altitudes above 220 km where data coverage was optimum and wind variations with altitude are reduced by viscosity (Hedin et al., 1988). Subsequent models, HWM90 and HWM93 then extended the formulation of HWM87 into the lower thermosphere, mesosphere and down to the surface of the Earth (Hedin and Biondi, 1991; Hedin et al., 1996). This extension was achieved by incorporating ground based data obtained from the COSPAR International Reference Atmosphere (CIRA-86) model plus rocket soundings, incoherent scatter radar, MF radar and meteor radar, and using lower-order spherical harmonics and Fourier series to describe major variations in the atmosphere (Hedin and Biondi, 1991; Hedin et al., 1996).

The revision of the previous horizontal wind model series saw an introduction of a new and improved HWM07 model. This model is comprised of two components; a geomagnetic quiet time component, for the background state of the atmosphere, and a geomagnetic active time component (DWM07), used to describe the winds' response to geomagnetic activity. HWM07 provides a statistical representation of the horizontal wind component of the Earth's atmosphere from the ground to the exosphere (0-500 km). This model is based on accumulated measurements made using a variety of observational techniques including satellite, radar and ground-based optical remote sensing (Drob et al., 2008). HWM07 was developed using compact FORTRAN subroutines. The input parameters for the computer model are: geographic location, altitude, day of the year, solar local time, and geomagnetic activity. The model is used to provide the necessary winds, accounting for time, space and geophysical variations, for many ionospheric, dynamical, and aeronomical calculations. This empirical model seeks to describe the dynamics of the atmosphere, not explain it (Rishbeth, 2007).

2.5 Summary

This chapter introduced instruments, models and their measurements that were utilized in this research. The Hermanus HF Doppler radar system was the primary source of data for analyzing Doppler frequencies and obtaining TID characteristics. GPS TEC measurements were used to compare and validate TID observations. TEC measurements were obtained by processing GPS RINEX files using a software developed by the Institute for Scientific Research at Boston College. The magnetic K index, derived from H-component measurements from the fluxgate magnetometer in Hermanus, was used to indicate the geomagnetic field conditions and validate the LSTID observations. The source code for HWM07 was run through

MATLAB by making use of a MEX-file. This model was used to validate the MSTID results observed from the HF Doppler radar data. The next chapter will focus on the data analysis tools and methods utilized to process the data obtained from the sources discussed in this chapter.

Chapter 3

Data Analysis Techniques

Several new tools and techniques were developed for the analysis of the dataset in order to meet the objectives of this thesis. This chapter is a layout of the primary analytic methods used while conducting the study.

3.1 HF Doppler data handling

HF Doppler data processing was mainly comprised of 2 stages; the pre-processing and the post-processing stage. IQ modulation, also referred to as Quadrature amplitude modulation (QAM), is a radio communication technique that sends two carrier waves with amplitudes in quadrature in order to reduce the signal to noise ratio. During the pre-processing stage, data were:

- IQ demodulated and combined,
- Smoothed by sliding a cosine window multiplied by a rectangular window of width, length of 15 minute time series/16,
- Displayed as spectrogram with the 3 traces from transmitting stations (refer to Figure 3.1)

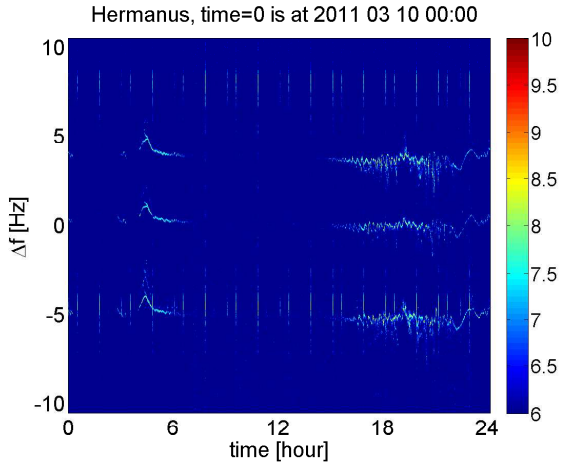

Figure 3.1: Whole day spectrogram recorded on the 10 March 2011.

The post-processing stage involved spectral analysis of the Doppler data. Initially, spectrograms were visually inspected for any signs of wave-like activity. The data would be windowed, around the observed structure, filtered and then processed. A third order Savitzky-Golay filter was applied to smooth the data. Unwanted frequency components of the data were removed by applying a wavelet bandpass filter with a bandwidth of 5 to 240 minutes (refer to Figure 3.2). Figure 3.2 illustrates a wave-like structure observed on all 3 traces of Doppler shifted frequencies. Thereafter, to acquire information about the period and propagation properties of the wave-like structure, spectral analysis was performed on the data using wavelet analysis described in Section 3.2. All processing of the data was performed on a MATLAB platform.

3.2 Wavelet Analysis

Wavelet analysis (also called wavelet theory or wavelets) is a digital signal processing technique suitable to study time varying, multiscale processing occurring over finite spatial and temporal domains (Lau and Weng, 1995). This technique allows one to decompose a time series into time-frequency space and hence, determine both dominant modes of variability and how those modes vary with time (Torrence and Compo, 1995). But unlike Fourier analysis, wavelet analysis decomposes its time series not in terms of trigonometric polynomials but in terms of wavelets generated in the form of translations and dilations of a fixed function called the mother wavelet (Lee and Yamamoto, 1994). A mother wavelet is a function whose set of

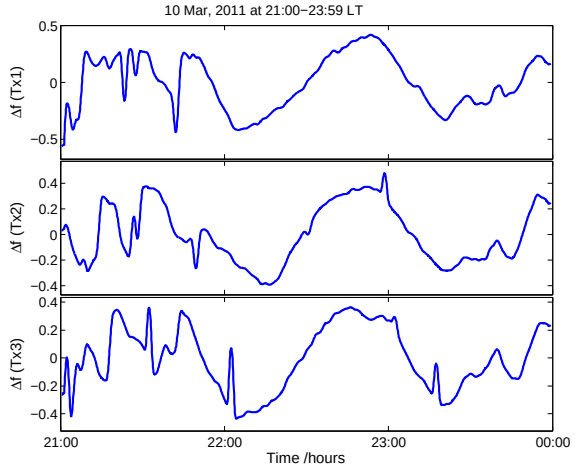

Figure 3.2: Whole day filtered spectrogram for data recorded on the 10 March 2011. Tx1, Tx2 and Tx3 are station codes for Worcester, Cape Town and Arniston receivers respectively.

discrete translations and dilations form an orthonormal basis, i.e. $\psi \in \mathbf{L}^2(\mathbb{R})$, where $\mathbb{R}$ is a set of real numbers and $\mathbf{L}^2$ is the set of all the functions, $\psi(t)$, which are fully integrable or have zero average (Equation 3.1) with finite energy (Equation 3.2), and are admissible (Equation 3.3) (Lee and Yamamoto, 1994; Mallat, 1998; Chun-Lin, 2010).

$$\int_{-\infty}^{\infty} \psi(t)\, dt = 0 \tag{3.1}$$

$$\int_{-\infty}^{\infty} |\, \psi(t)\, |^2\, dt < \infty \tag{3.2}$$

$$C_\psi = 2\pi \int_{-\infty}^{\infty} \frac{|\, \Psi(\omega)\, |^2}{|\, \omega\, |}\, d\omega < \infty \tag{3.3}$$

where Ψ is the Fourier transform of ψ. These wavelets are localized both in time and in frequency, allowing a closer connection between the time series and its coefficients.

Since its introduction the wavelet analysis technique has been preferred to other digital signal processing (DSP) techniques because of its capability to revealing aspects of data like trends, breakdown points, and self-similarity that other signal analysis techniques omit. Therefore this technique was used to measure periods and propagation properties of these perturbations.

3.2.1 Continuous wavelet transform

Using the scaling and shifting property, the general expression for the mother wavelet can be denoted by

$$\psi_{s,u}(t) = \frac{1}{\sqrt{s}}\psi\left(\frac{t-u}{s}\right) \tag{3.4}$$

where $u \in \mathbb{R}$ is the shifting parameter, $s \in \mathbb{R}_+$ is the scaling parameter greater than zero because negative scaling is undefined and $(s)^{-1/2}$ is the energy normalization factor. Using Equation (3.4), assuming it satisfies the conditions given by Equations (3.1) and (3.2), a continuous wavelet transform (CWT) of a time series, $f(t)$, with respect to the wavelet function, $\psi(t)$, may be defined as a convolution integral:

$$\begin{aligned} W(s,u) &= \int_{-\infty}^{\infty} f(t)\,\psi^*_{s,u}(t)\,dt \\ &= \int_{-\infty}^{\infty} f(t)\,\frac{1}{\sqrt{s}}\psi^*\left(\frac{t-u}{s}\right)dt \end{aligned} \tag{3.5}$$

where ψ^* is the complex conjugate of ψ. This transform maps a one-dimensional signal, $f(t)$, to a two-dimensional coefficients' matrix, $W(s,u)$ using Equation (3.5), allowing a particular frequency (parameter s) to be determined at a certain time instant (parameter u). This transform works when a continuous wavelet function is used to find the detailed coefficients of a continuous signal. Wavelet functions are designed to strike a balance between the time domain of a finite length and the frequency domain of a finite bandwidth of a time series. During the scaling and translation of the mother wavelet, one can observe very low frequency components at large s while very high frequency components can be located precisely at small s (Chun-Lin, 2010).

If the function, $\psi(t)$, satisfies admissibility conditions (Equation 3.3) and $f \in \mathbf{L^2}(\mathbb{R})$, then the original time series signal, $f(t)$, can be reconstructed from the transform $W(s,u)$using the following inverse formula:

$$f(t) = \frac{1}{C_\psi}\int_0^{\infty}\int_{-\infty}^{\infty} W(s,u)\,\frac{1}{\sqrt{s}}\psi\left(\frac{t-u}{s}\right)du\frac{ds}{s^2} \tag{3.6}$$

Several types of wavelet basis functions are in existence to date but the most commonly used are Daubechies, Haar, Maxican hat, Meyer and Morlet. These basis functions are either real or analytic, and depending on their applications real wavelets are often used to detect sharp signal transitions whereas analytic wavelets are used to measure the time evolution of frequency tones of a time series. An analytic wavelet is a function whose Fourier transform is zero for negative frequencies (Mallat, 1998, p. 81):

$$\Psi(\omega) = 0 \quad \text{if} \quad \omega < 0$$

Analytic functions are necessarily complex but entirely characterized by the real part. The use of a complex analytic wavelet such as a Morlet wavelet function makes it possible to measure the time evolution of frequency transients of a time series by separating the amplitude and phase components (Mallat, 1998; Bloomfield et al., 2004). A Morlet wavelet is approximately a Gaussian function modulated by a sine wave and is given by the following:

$$\psi(t) = \pi^{-1/4} e^{i\omega_0 t} e^{-t^2/2} \tag{3.7}$$

with its Fourier transform expressed as:

$$\Psi(\omega) = \pi^{-1/4} H(\omega)\, e^{-(s\omega-\omega_0)^2/2} \tag{3.8}$$

where ω_0 is the fundamental frequency of the wavelet and

$$H(\omega) = \begin{cases} 1 & \text{if } \omega > 0 \\ 0, & \text{otherwise} \end{cases}$$

is the Heaviside step function (Torrence and Compo, 1995). The Morlet wavelet best suited this research because it provided useful information about the amplitude and phase relation on a pair of HF signals from different transmitting locations that are reflected by the ionosphere. Another advantage of using a Morlet wavelet is that its scales are directly related to the Fourier period (Period = $1.03s$). Figure 3.3 demonstrates a complex Morlet function with the center frequency equal to 6 radians per second. For the purpose of this research, this value was chosen because it gave the optimum result for time-frequency resolution. Figure 3.4 illustrates scalograms obtained after performing CWT on the structures observed on 10

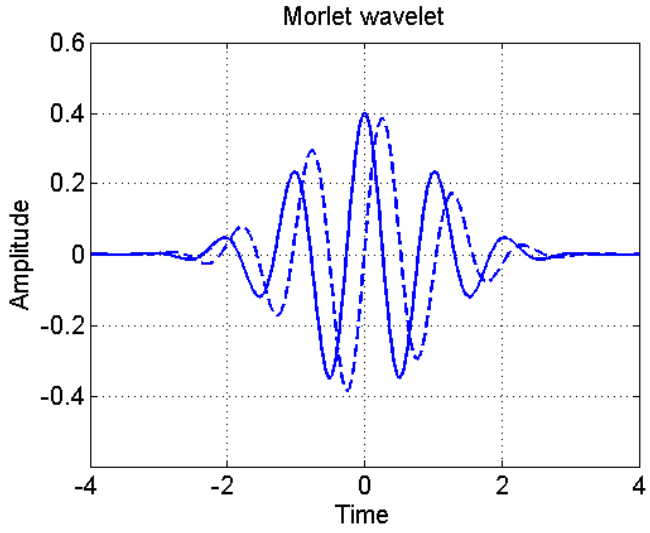

Figure 3.3: Complex Morlet wavelet ($\omega_0 = 6$) with the real part (solid) and the imaginary part (dashed).

March 2011 (refer to Figure 3.2) using Equation (3.5). The blue trace to the right of the scalogram exemplifies the wavelet power spectra, WPS, computed at each scale. The power spectra illustrated dominant coefficients as a function of scales, s, at each time, u. The scale value at each WPS peak signifies a period of the wave-like structure observed at a particular instant of time, u.

3.2.2 Wavelet Cross Spectrum

Liu (1994) defined the wavelet cross spectrum (WCS) of a biviriate data $x(t)$ and $y(t)$ as the expectation value of the product of the corresponding wavelet transforms, $W_x(s,u)$ and $W_y(s,u)$:

$$\begin{aligned} W_{xy}(s,u) &= \left\langle W_x(s,u)\, W_y^*(s,u) \right\rangle \\ W_{xy}(s,u) &= \left| W_{xy}(s,u) \right| e^{i\Phi(s,u)} \end{aligned} \tag{3.9}$$

WCS is complex valued and hence, it can be decomposed into amplitude, $\left|W_{xy}(s,u)\right|$, and phase difference. Equation (3.9) is the measure of covariance between two time series $x(t)$

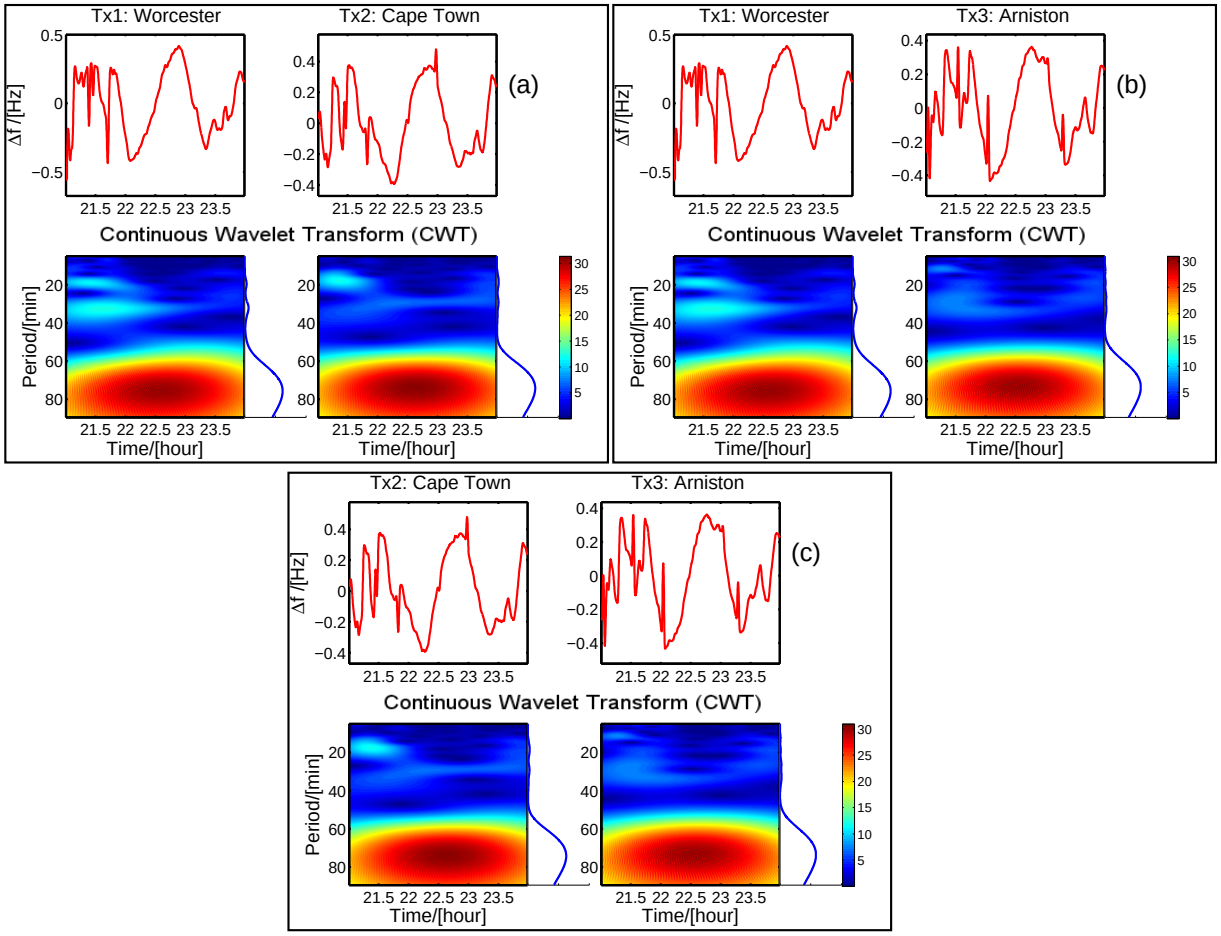

Figure 3.4: CWT scalograms for the data recorded on the 10 March 2011.

and $y(t)$. This equation was used to determine the dominant scales of the of the structures observed in the time series. By locating the dominant scale and summing the WCS at that particular scale across time, Schmidt and Schuh (2000) defined the wavelet cross-covariance of two stochastic time series $x(t)$ and $y(t)$ using the formula

$$C_{xy}(s,\beta) = \int_{-\infty}^{\infty} W_x(s,u)\, W_y^*(s,u+\beta)\, du \tag{3.10}$$

and the time lag function, $\beta(s)$, using the condition

$$\beta(s) = \underset{\beta \varepsilon \mathbb{R}}{\arg\max} \left| C_{xy}(s,\beta) \right| \tag{3.11}$$

Equation (3.11) was used to determine the time lag at a scale obtained from Equation (3.9). Further details about the cross-covariance can be obtained from Schmidt and Schuh (2000). In the study undertaken, Equation (3.11) was used to obtain the time delay of an event structure observed in two time series $x(t)$ and $y(t)$. Figure 3.5 demonstrates wavelet cross spectra scalograms obtained by multiplying the CWT coefficients' matrix of one signal with complex conjugate of the CWT coefficients' matrix of another signal, using Equation (3.9). The spectrograms illustrated periods of the time series events with dominant energy. The global wavelet spectrum (GWS), represented by the sub-figure to the right of the scalogram, is the time average of the wavelet coefficients normalized by the variance at each scale. The period, T, of the observed TIDs was obtained by taking the scale values at the GWS peaks. The mean time delay of a structure observed between signals from two transmitting stations was determined using Equation (3.11). Equation (3.12) was used to compute the distance, in km, between the transmitter and the receiver.

$$\begin{aligned} dx &= \frac{lon1 - lon2}{2} \times \frac{\cos lat1 + \cos lat2}{2} \times R \\ dy &= \frac{lat1 - lat2}{2} \times R \end{aligned} \tag{3.12}$$

where:

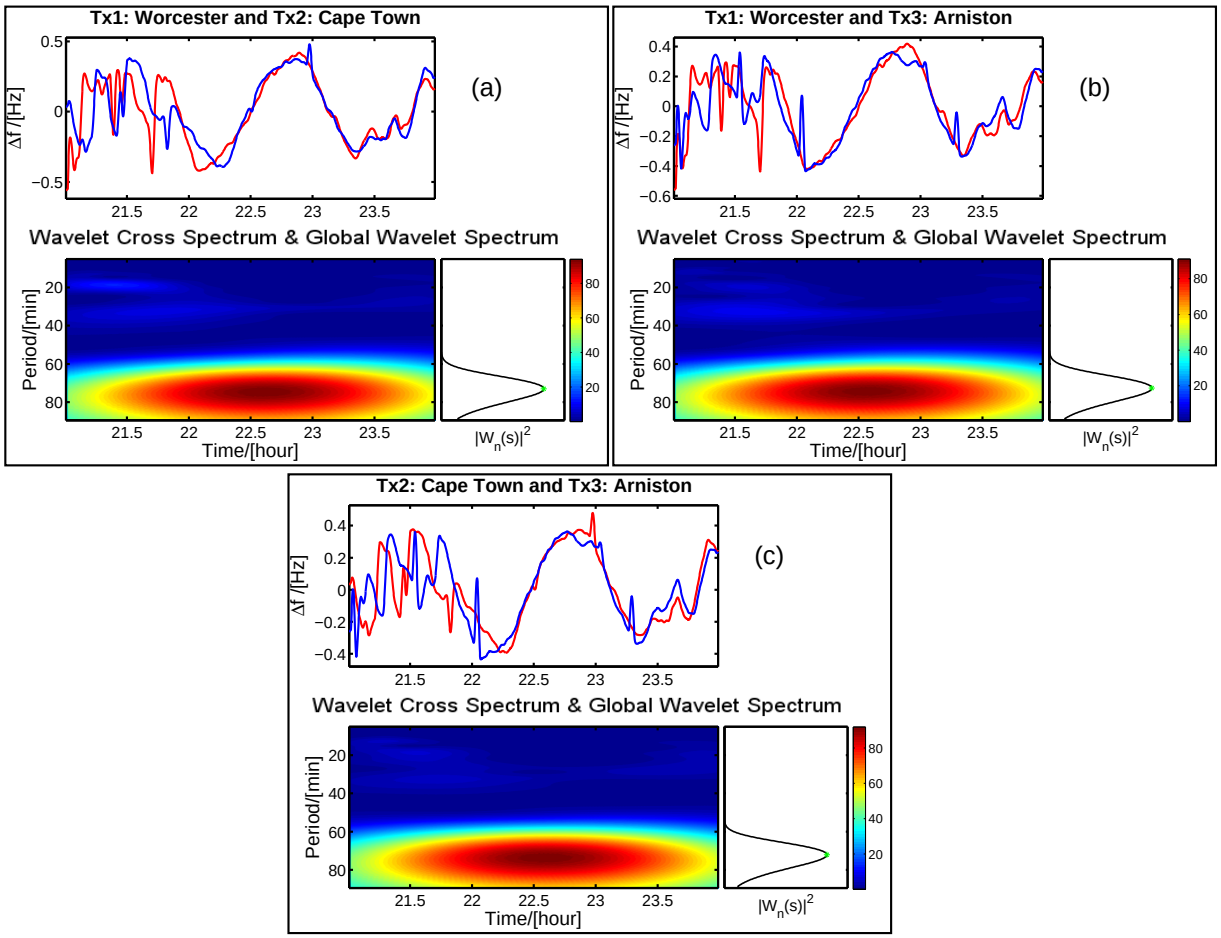

Figure 3.5: WCS and Global wavelet spectra (GWS) scalograms for the data recorded on the 10 March 2011, with the time window: 21:00-00:00.

R = 6371000 m is the mean Earth radius

lat1, lat2 = latitudes of 1^{st} and 2^{nd} transmitters respectively

lon1, lon2 = longitudes of 1^{st} and 2^{nd} transmitters respectively

dx = distance in the East-West direction in m

dy = distance in the North-South direction in m

The mean velocity, v , of the observed TID was determined by dividing distance between the transmitter and the receiver by the time delay. The azimuth, ϑ, of propagation of the observed TIDs was evaluated using the following:

$$\vartheta = \begin{cases} 90^\circ - \frac{180}{\pi}\tan^{-1}\left(\frac{v_y}{v_x}\right), & \text{if} > 0 \\ 180^\circ + 90^\circ - \frac{180}{\pi}\tan^{-1}\left(\frac{v_y}{v_x}\right), & \text{otherwise} \end{cases} \tag{3.13}$$

where v_x and v_y are the x and y components of the TID propagation velocity, v, in ms^{-1}. The wavelength, λ, of the observed structure was determined using Equation (3.14).

$$\lambda = vT \tag{3.14}$$

Table 3.1: Spectral analysis for the event observed on 10 March 2011 21:00 - 23:59

Path	Time	dt/[min]	d/[km]	v/[m/s]	T/[min]	$\lambda/[km]$	$\alpha/[^\circ]$
Wor-Cap:	22:34	-1.8336	47.80	434.53	77.00	2007.53	70.1
Wor-Arn:	22:32	-2.7377	66.31	403.69	76.00	1840.83	323.4
Cap-Arn:	22:35	-0.9653	91.92	1587.08	76.00	7237.08	293.7

Path = transmitter pairs (Worc, Cap and Arn →Worcester, Cape Town and Arniston respectively), Time = time at half-the-period of the event, dt = time delay between respective signal paths, d = midpoint distance between the transmitter pair in km, v = velocity of the TID structure in m/s, T = period of the observed structure in minutes, λ = wavelength in km and α = azimuth clockwise from the geographic North.

Results obtained from spectral analysis of the event that was recorded on the 10 March 2011 are tabulated in Table 3.1. This is a typical output of spectral analysis of the observed TID events. Transmitter pairs in the first column indicate the GPS transmitted signals

used for cross-spectral analysis for each transmitter station pair (e.g. Worcester-Cape Town, Worcester-Arniston and Cape Town-Arniston). The parameters such as time of occurrence, time delay, distance velocity, period, wavelength and azimuth computed for each station pair are listed.

3.3 SADM-GPS algorithm

The statistical angle of arrival and Doppler method for GPS interferometry (SADM-GPS) is the processing technique utilized to measure the GPS signal interference pattern. This method was developed at the Institute of Solar-Terrestrial Physics, Siberian Division, Russian Academy of Science (Afraimovich, 2000). The method has been used to study both MSTIDs and LSTIDs. SADM-GPS is an extension to the work done by Mercier (1986) while studying atmospheric gravity waves using radio-interferometry. He suggested that perturbations in the Earth's ionosphere could be investigated using ground-based radio-interferometric techniques. By making use of the apparent position shift of a radio source observed with a two dimensional radio-interferometer, he argued that, one could directly obtain the two components of the horizontal gradient of the sTEC, and thus obtain the propagation azimuth of gravity waves. Mercier's (1986) method for deducing the gravity wave propagation azimuth involved determining a series of instantaneous values of the azimuth using the following equation:

$$\alpha(t) = \tan^{-1}\left(\frac{\phi'_y(t)}{\phi'_x(t)}\right) \tag{3.15}$$

where ϕ'_x and ϕ'_y are first phase derivatives with respect to the spatial coordinates x and y at the reception point proportional to the angles of arrival variations. The mean value of $\alpha(t)$ is then used to estimate the azimuth of the prevailing interference pattern. Afraimovich (1995, 1997) expanded on the Mercier (1986) interferometry algorithm. He proposed the statistical angle of arrival and Doppler method (SADM) for determining the characteristics of the dynamics of the phase interference pattern in the horizontal plane by including information about the time derivative of the phase, $\phi'_t(t)$, proportional to the frequency Doppler shift variations.

This allowed for the determination of the velocity, $u(t)$, at each specific instant in time.

$$\begin{aligned} u_x(t) &= \frac{\phi_t'(t)}{\phi_x'(t)} = u(t)\cos\alpha(t) \\ u_y(t) &= \frac{\phi_t'(t)}{\phi_y'(t)} = u(t)\sin\alpha(t) \\ u(t) &= \frac{\left|u_x(t)\,u_y(t)\right|}{\sqrt{u_x^2(t)+u_y^2(t)}} \end{aligned} \tag{3.16}$$

Afraimovich et al. (1998, 1999) updated the SADM algorithm for GPS arrays based on the model for the displacement of the phase interference patterns that travel without losing shape with regard to the motion of the satellite. Equation (3.16) was corrected by subtracting the ionospheric pierce point (IPP) (refer to Figure 2.7) velocity, $w(t)$, to remove effects of the satellite motion. The SADM-GPS algorithm expression, $V_h(t)$, is then given by the following:

$$V_h(t) = u(t) + w_x(t)\sin\alpha(t) + w_y(t)\cos\alpha(t) \tag{3.17}$$

where w_x and w_y are the x and y projections of the velocity, $w(t)$, of the IPP. He made use of the SADM-GPS algorithm, in conjunction with the multi-satellite GPS radio interferometry, to work out the velocity vector of TIDs in the entire azimuthal range of possible propagation directions. This method has been widely used for TID studies using GPS data, for example see (e.g. Afraimovich et al., 1999; Afraimovich, 2000; Afraimovich et al., 2003; Perevalova et al., 2008; Valladares and Hei, 2012). In this study, the SADM-GPS method was used to validate some of the observed TIDs' propagation properties such as speed and direction.

3.4 Summary

This chapter has discussed the primary tools and techniques used for the analysis of data obtained using methods described in Chapter 2. The wavelet analysis technique is a very useful tool, used in digital time series processing, and has become more popular in the last century. It has been chosen for this study because of its ability to resolve a time series both in frequency and in time, divulging features missed by other techniques. The SADM-GPS algorithm is a great tool for determining perturbations in the ionosphere using GPS TEC as it subtracts the effects of satellite motion, giving more precise information about TIDs from GPS TEC. The next chapter focuses primarily on the interpretation of the results obtained from the HF Doppler dataset, while comparing results from other datasets discussed in Chapter 2.

Chapter 4

Results

The primary focus of this chapter is on the analysis and interpretation of the Hermanus HF Doppler radar dataset. To validate the HF Doppler radar results GPS TEC data were used. The local K index was used to verify magnetic activity around the time of observation of LSTIDs. The results presented herein were obtained from the analysis of datasets discussed in Chapter 2 using tools and techniques covered in Chapter 3.

4.1 Spatial and temporal characterization of TIDs

Figure 4.1 illustrates the Doppler shifted frequency spectrograms for selected dates in 2010, 2011 and 2012. These dates; 22 January 2012, 10 March 2011, 06 June 2012 and 16 September 2010 , were chosen to illustrate the characteristics of the observed TIDs during different seasons. TIDs were only observed during the local morning and evening times; note local time is universal time (UT) + 2 hours. The traces in all four spectrograms exhibit a significant degradation around noon which is associated with the HF radio absorption by the *D* region (Beer, 1974). This was the case with all the data for the whole duration of the study. Another limiting factor for TID observation was a complete signal loss which occurred in the early morning and late night hours, mostly observed during local winter (e.g Figure 4.1d). This was mostly due to a low F2 critical frequency; i.e. foF2 being lower than the sounding frequency of 3.59 MHz. The critical frequencies of the ionosphere were recorded using a digisonde located nearby (i.e. located in Hermanus ($34^{\circ}25'30''S$, $19^{\circ}13'30''E$)). Figure 4.2

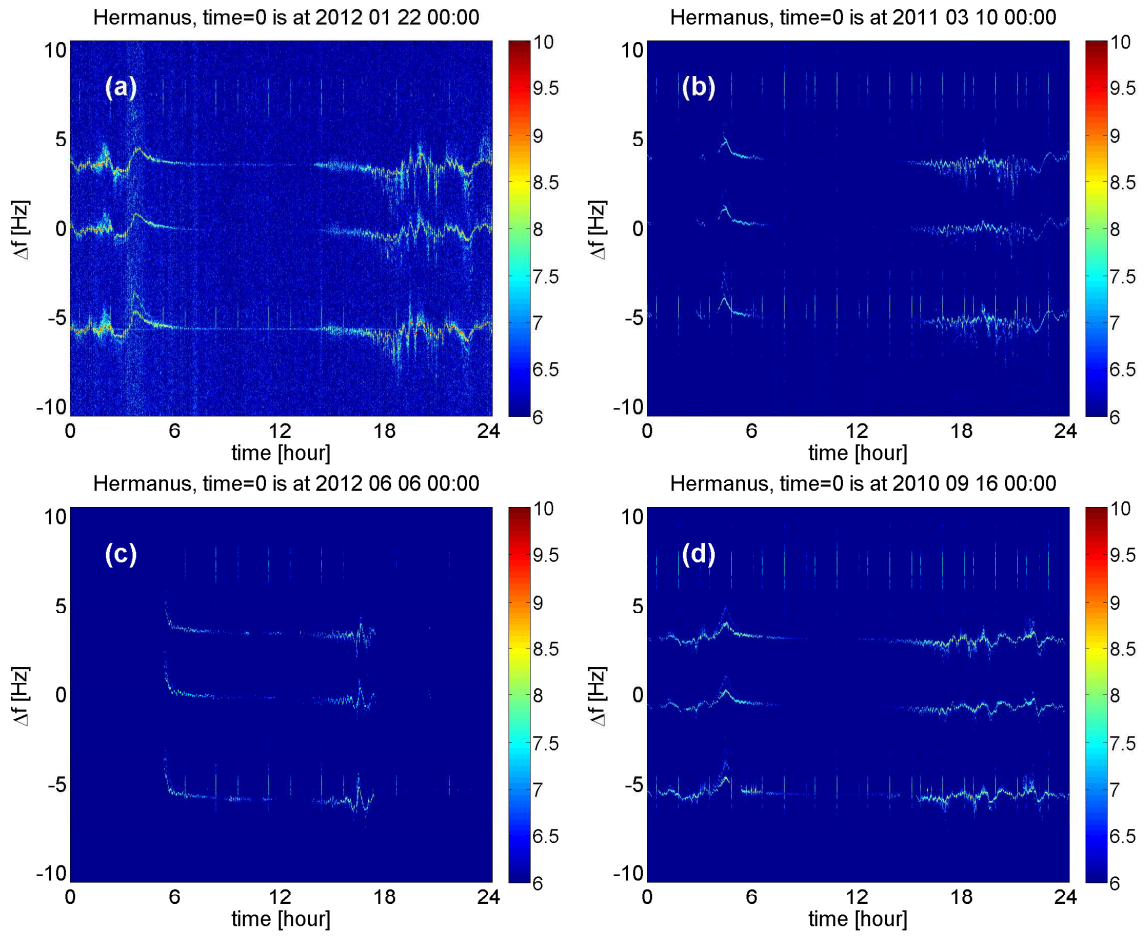

Figure 4.1: Spectrograms for (a) January 2012; (b) March 2011; (c) June 2012; and (d) September 2010.

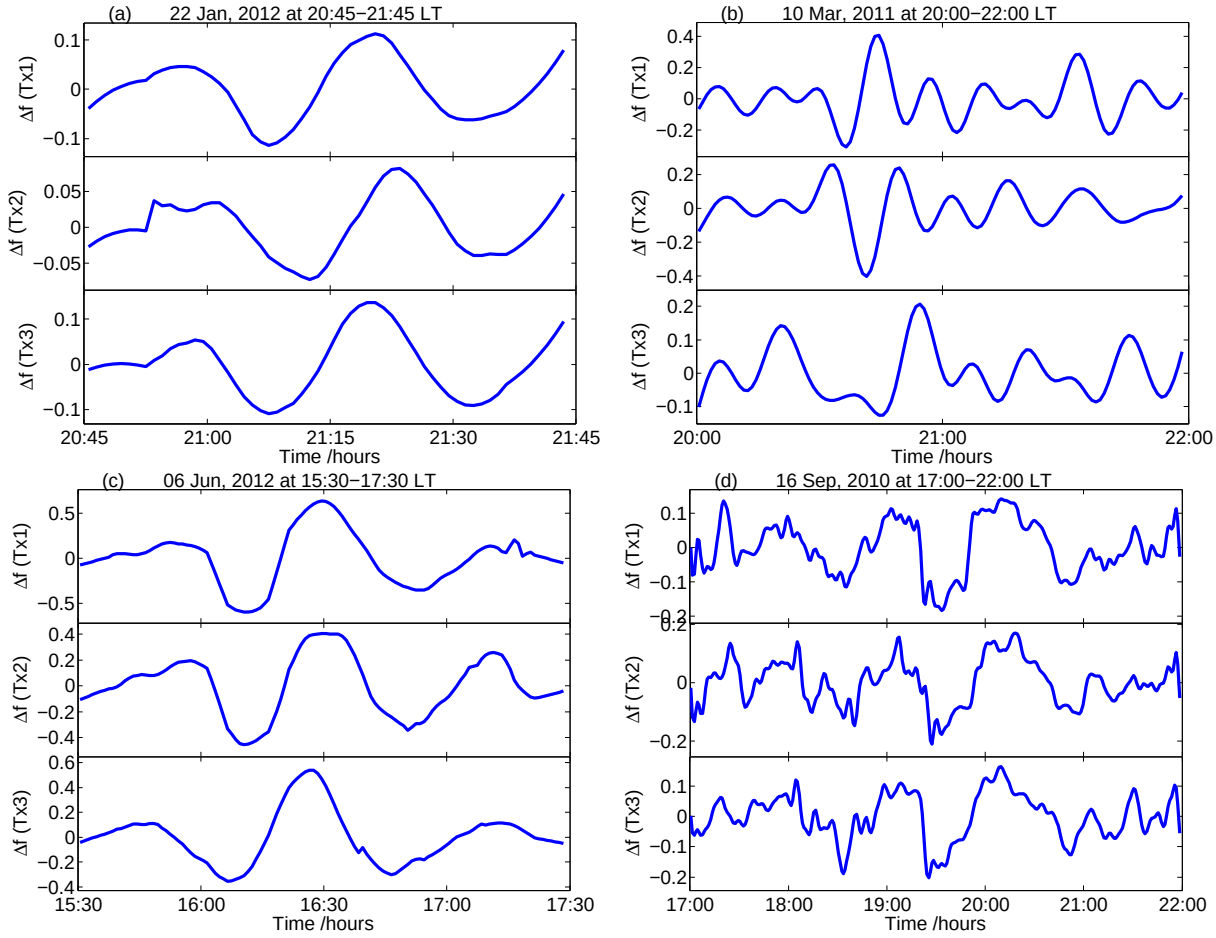

Figure 4.2: Peak frequency versus time for the event times extracted from Figure 4.1 (a-d).

exemplifies some of the TID events observed for the selected dates. Only wave-like perturbations with periods of 10 - 180 minutes were considered for the study. Perturbations with periods of approximately 10 - 40 minutes and speeds less than 400 m/s were classified as MSTIDs, whereas perturbations with periods of approximately 40 - 180 minutes and speeds larger than or equal to 400 m/s were classified as LSTIDs. Discussed hereafter are the events observed from Figure 4.2 (a-d) that were analyzed using techniques discussed in Chapter 3.

On the 22 January 2012 a wave-like perturbation was detected at 20:45 - 21:45 LT (refer to Figure 4.2a). A MSTID structure with the period of 24 minutes (Figure 4.3a) and a wavelength of approximately 569.5 km was observed travelling due northwest (azimuth of 277.0°) with the speed of approximately 395.5 m/s.

Figure 4.2 (b) exemplifies a quasi-periodic perturbation observed from all 3 traces at 20:00 - 22:00 LT on 10 March 2011. Spectral analysis revealed periods for two structures (Figure

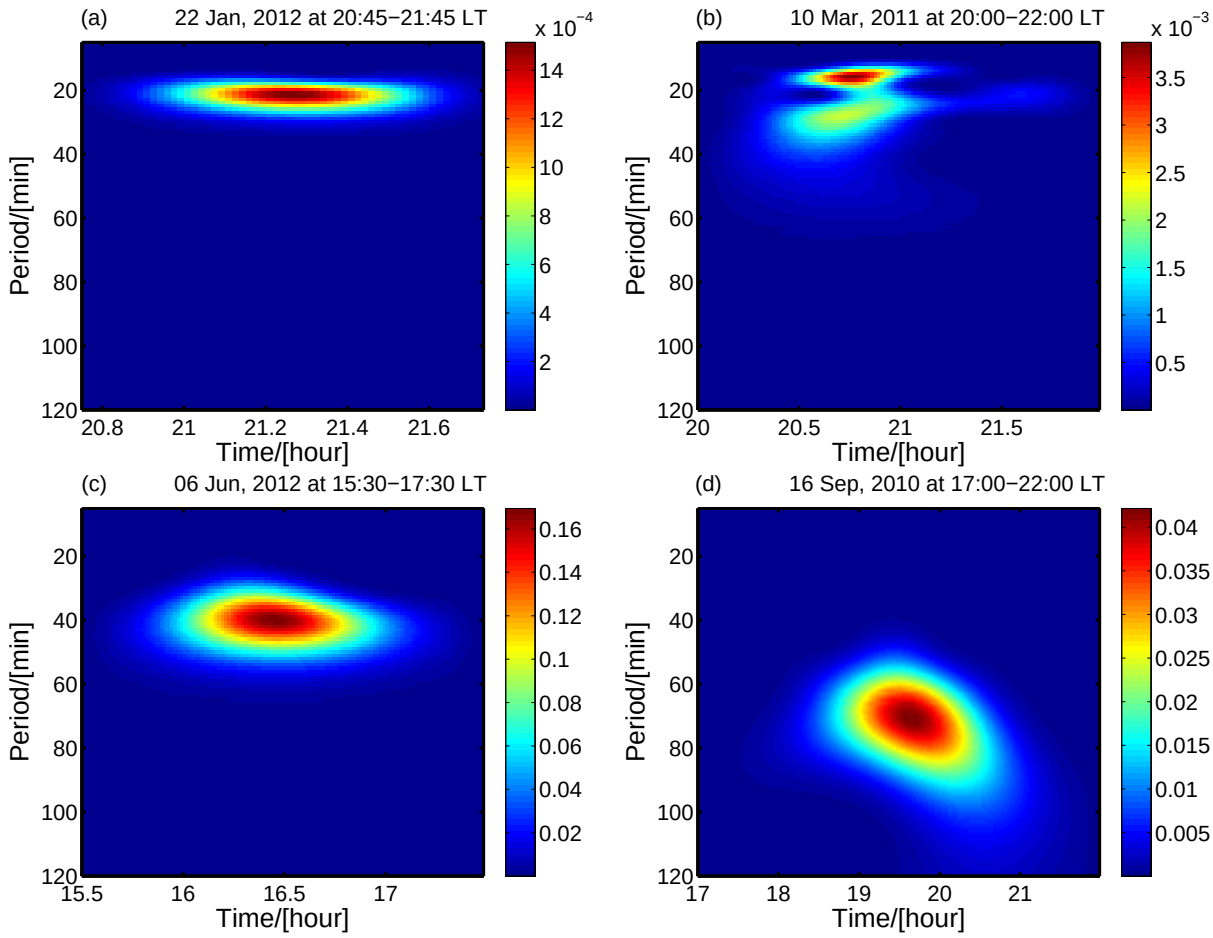

Figure 4.3: Wavelet spectrograms illustrating periods of the observed TID events, extracted from Figure 4.1 (a-d).

4.3b). The first MSTID, with a period of 15 minutes and a wavelength of approximately 169 km, was observed propagating with an average speed of 187.9 m/s at an azimuth of 286.7°; and the second MSTID, with a period of 26 minutes and a wavelength of approximately 515 km, was observed moving with a mean speed of 329.8 m/s at an azimuth of 218.6°.

A quasi-periodic fluctuation is demonstrated in Figure 4.2 (c), which is an extraction from Figure 4.1 (c), at 15:30 -17:30 LT on 06 June 2012. This wave packet, with a period of 42 minutes and wavelength of approximately 720 km, was detected travelling with a mean speed of 282.6 m/s. The parameters suggested that the wave packet was a MSTID propagating northwestward at an azimuth of 308.5° from the geographic north.

A close inspection of Figure 4.1 (d) reveals fluctuations in the peak frequency in the evening hours of 16 September 2010 between 17:00 and 22:00 LT. The spectral analysis in Figure 4.2 (d) reveals a structure with a period of 72 minutes (Figure 4.3d) and a wavelength of approximately 6989 km. This LSTID was observed moving westward (azimuth of 271.9°) with an average speed of 1634.7 m/s.

MSTID events observed during solstices (22 January 2012 and 06 June 2012) are stronger, in terms of speed and wavelengths, when compared to the first MSTID event recorded on the 10 March 2011. The second MSTID event recorded on the 10 March 2011 has velocity and period values comparable with those recorded on 22 January 2012. All the studied structures, discussed in the examples above, appeared to have a west-northwest preferred direction of propagation. The results from the above mentioned examples are not enough to make a conclusion on the seasonal dependency of TIDs.

4.1.1 Statistical Analysis

A summary of seasonal propagation properties of observed TIDs over the southwestern region of South Africa from May 2010 until June 2012 is presented in Table 4.1. The results are summarised seasonally for both the daytime (AM) and the nighttime (PM) periods. AM indicates times between 00:00 and 12:00 LT, and PM indicates times between 12:00 and 23:59 LT. The results are analysed as follows:

There were more daytime MSTIDs observed than nightime MSTIDs for mostly all seasons except winter where this trend was the reverse. There were slightly higher MSTIDs observed

Table 4.1: Summary of TIDs characteristics obtained for the period, 2010-2012.

Season	TIDs class	N	$\bar{v}$/[m/s]	v_m/[m/s]	σ_v/[m/s]	$\bar{\alpha}$/[°]	σ_α[°]
Autumn	MSTIDs, AM	52	198.6	196.9	51.8	213	60
	PM	31	184.7	186.9	67.8	181	72
	LSTIDs, AM	8	741.8	615.4	357.0	198	86
	PM	23	624.6	548.6	301.4	156	64
Winter	MSTIDs, AM	21	206.3	203.6	45.7	209	71
	PM	45	205.8	210.6	56.5	197	67
	LSTIDs, AM	0	-	-	-	-	-
	PM	0	-	-	-	-	-
Spring	MSTIDs, AM	57	198.9	196.6	57.2	204	74
	PM	17	163.0	161.9	68.7	191	66
	LSTIDs, AM	15	881.9	674.1	546.7	198	76
	PM	23	696.0	539.6	418.7	170	76
Summer	MSTIDs, AM	52	189.7	192.7	59.4	218	70
	PM	21	160.9	151.8	63.1	184	60
	LSTIDs, AM	6	607.2	546.0	288.2	189	99
	PM	10	641.3	524.6	368.3	195	74

N = number of observations, $\bar{v}$ & v_m = mean and median velocities respectively, σ_v = standard deviation of velocities, $\bar{\alpha}$ = mean azimuth and σ_α = standard deviation of azimuths.

in autumn and spring than in winter and summer. Winter MSTIDs, both daytime and nighttime MSTIDs, were generally fastest when compared to the rest of the seasons. For spring, autumn, winter and summer; daytime MSTIDs propagated with similar average speed. The difference in speeds is observed when looking at the nighttime MSTIDs, with winter having a slightly higher value.

Nighttime LSTIDs were more than the daytime LSTIDs for all the seasons, except winter when there were no LSTIDs observed. There were slightly more LSTIDs observed in spring, with summer having the lowest number of observations. Daytime and nighttime LSTIDs observed during spring were faster than the LSTIDs observed during autumn and summer. The general direction of propagation for autumn and spring nighttime LSTIDs was towards south-southeast, with the daytime LSTIDs generally propagating south-southwest. There were no LSTIDs observed during winter.

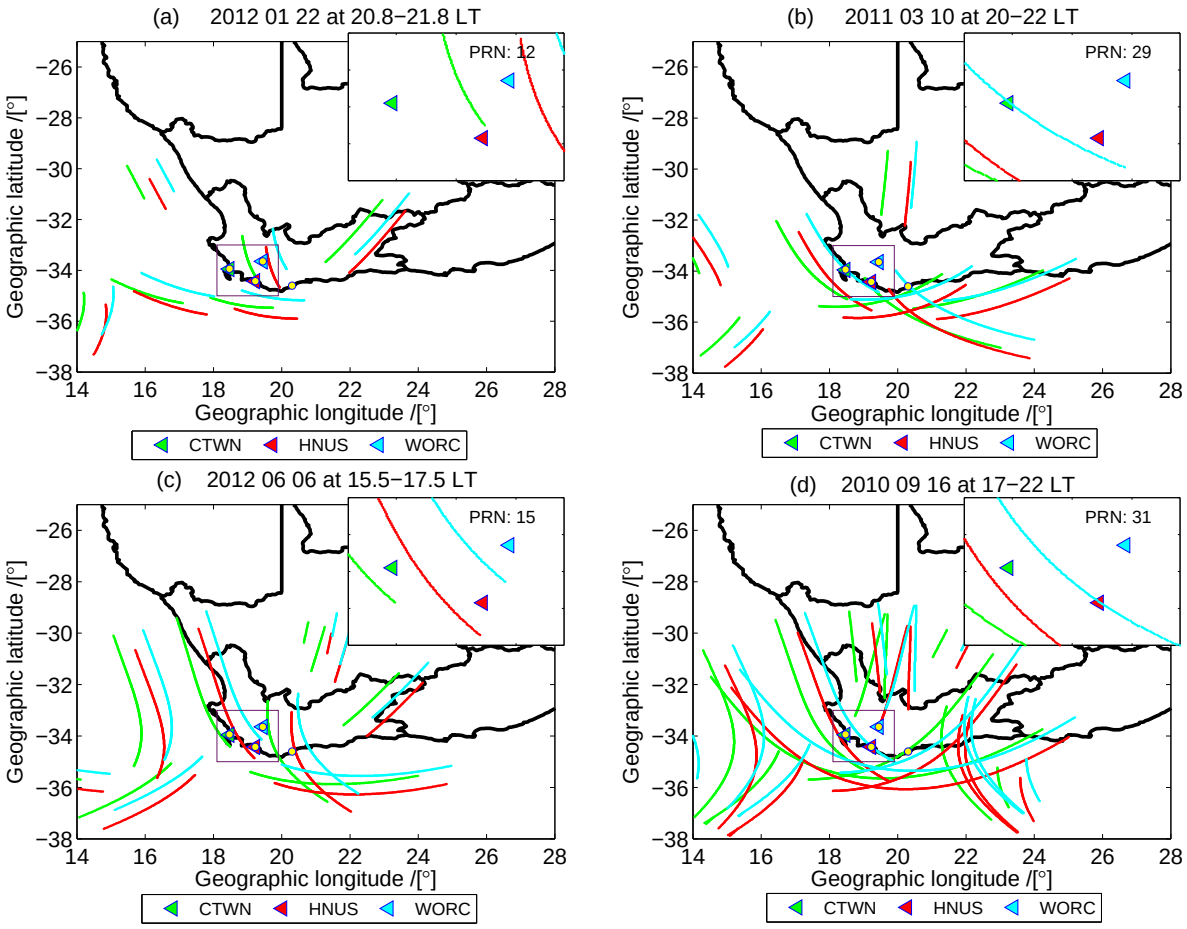

Figure 4.4: IPP trajectories of individual PRNs as seen by each of the 3 GPS receiver stations at the times of TID events. Yellow filled circles represent the HF Doppler radar receiver-transmitters network. The insert is a magnification of the area around the receivers showing the IPP trajectory of a PRN passing closest to the GPS receivers.

4.2 GPS TEC validation

GPS TEC dataset was used to validate the TIDs' results presented in Section 4.1. The GPS receiver stations, located in Hermanus, Cape Town and Worcester, were selected to be in the vicinity of the HF Doppler radar transmitters-receiver network (refer to Table 4.2) to ensure they record the same events. Figure 4.4 (a-d) illustrates satellites that were visible to all three GPS receivers at the times of observation of TID events (refer to Figure 4.2 a-d) by means of IPPs. The yellow filled circles represent the HF Doppler radar stations. For this example PRN 13 TEC, with IPP trajectory closest to the GPS receivers, was selected. The insert on the right-hand corner illustrates a magnified GPS receiver array with PRN 13 IPP trajectories, as seen

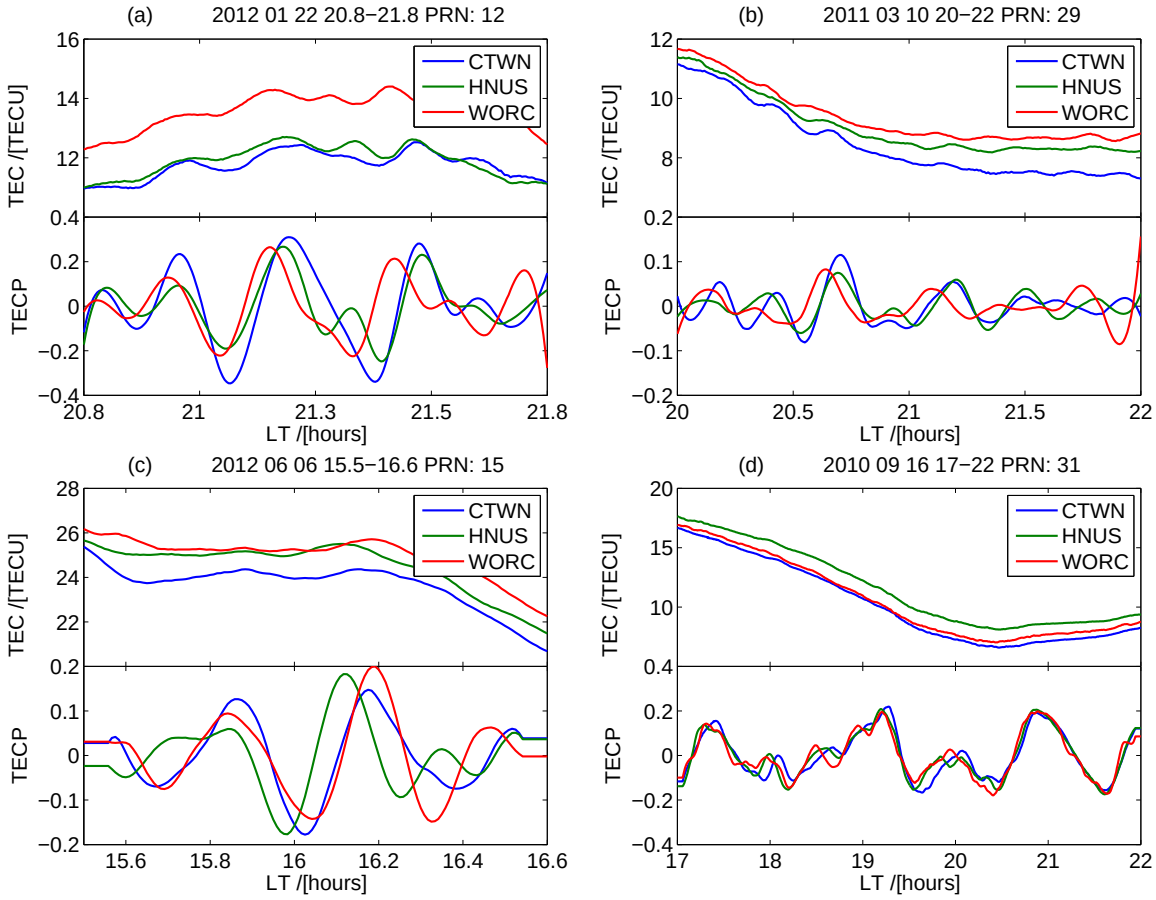

Figure 4.5: TEC perturbations for the TIDs discussed in Section 4.1.

by each receiver indicated. Elevation angles greater than 30° were chosen when selecting PRN data in order to avoid multipath. Multipath is a contamination of a GPS signal that is caused by the reflection and refraction from the surrounding surfaces of the GPS receiver antenna (Hannah, 2001; Larson et al., 2007). The equivalent vTEC at an average IPP altitude of 350 km was calculated assuming the ionospheric thin shell model. Figure 4.5 illustrates TEC perturbations for the times around the TID events that were discussed in Section 4.1. The perturbations were determined by detrending vTEC. This was done by subtracting the 6^{th} order polynomial from the vTEC. This value of the polynomial order was selected because it gave the best fit to the GPS TEC data. Dominant spectral components of the analyzed events were obtained by making use of the wavelet analysis technique. The TEC TIDs' propagation properties were determined using the SADM-GPS algorithm (detailed in Section 3.3).

In Figure 4.5 (a), a perturbation in PRN 12 TEC is detected between 21:00 and 23:00 LT (19:00 - 21:00 UT) on the 22 January 2012. Spectral analysis revealed a structure with the

Table 4.2: GPS receiver and HF Doppler radar stations.

GPS/HF Doppler station	Station Code	Geographic Latitude /[°]	Geographic Longitude /[°]
HF Doppler radar network:			
Worcester	Tx1	-33.65	19.44
Cape Town	Tx2	-33.94	18.47
Arniston	Tx3	-34.60	20.30
Hermanus	Rx	-34.43	19.23
GPS receiver network:			
Hermanus	HNUS	-34.42	19.22
Cape Town	CTWN	-33.95	18.47
Worcester	WORC	-33.64	19.45

period of 21 minutes and a wavelength of approximately 410 km moving northwestward (azimuth of 272°) with a mean speed of 325.1 m/s.

A TEC perturbation on PRN 29 that reached a maximum amplitude of approximately 0.1 TECU (refer to Figure 4.5b) was detected by all 3 GPS receivers on the 10 March 2011 at 20:00 - 22:00 LT (18:00 - 20:00 UT). Wavelet analysis revealed two structure periods of 16 and 28 minutes. The MSTID with a period of 16 minutes and a wavelength of 163.3 km was propagating due northwest (azimuth of 293°) with a mean speed of 201.4 m/s. On the other hand, the MSTID with the period of 28 minutes and a wavelength of approximately 607 km was moving southwestward (azimuth of 196°) with an average speed of 361.5 m/s.

Figure 4.5 (c) illustrates PRN 15 TEC recorded on the 06 June 2012 at 15:30 - 16:36 LT (13:30 - 14:36 UT). Fluctuations are observed on TEC and when detrended, the fluctuations are clearly visible having a maximum amplitude of approximately 0.2 TECU. Spectral analysis revealed a MSTID, with a period of 21 minutes and a wavelength of approximately 609.8 km, that was travelling northwestward (azimuth of 298°) with an average speed of 487.6 m/s.

Figure 4.5 (d) illustrates PRN 13 TEC recorded on 16 September 2010 at 17:00 - 20:00 LT

Table 4.3: Summary of Doppler radar versus GPS TEC LSTIDs results for the selected events.

Instrument	Date of observation	Time [UT+2]	$\bar{v}/[m/s]$	σ_v	$T/[min]$	$\bar{\lambda}/[km]$	σ_λ	$\alpha/[^\circ]$	σ_α
R	22/01/2012	20:45-21:45	395.5	127.7	24	569.5	255.7	277.0	29.8
G			325.1	161.1	21	409.6	203.0	271.9	30.8
R	10/03/2011	20:00-22:00	187.9	17.8	15	169.0	117.9	286.7	60.5
			329.8	62.3	26	514.5	73.5	218.6	88.7
G			201.4	46.3	16	193.3	66.9	293.5	73.2
			361.5	70.1	28	607.3	208.2	195.6	67.6
R	06/06/2012	15:30-17:30	282.6	45.0	42	719.6	102.7	308.6	21.0
G		15:30-16:36	487.6	125.5	21	609.8	128.0	298.1	54.2
R	16/09/2010	19:00-21:00	1634.7	467.4	72	6989.5	916.2	271.9	92.0
G			-	-	-	-	-	-	-

R, G = Doppler Radar and GPS TEC data respectively.

(15:00-18:00 UT). Although no wavelike structures were observed in the TEC data, wavelike structures are detected in the detrended data. One must keep in mind that the 6th order polynomial is not a perfect approximation of the TEC variability and therefore there will be some sinusoidal residue between the polynomial and the TEC measurements. The structures in the detrended data were therefore deemed unreliable and spectral analysis and velocity measurements could not be ascertained. However this was the only PRN visible during the period of TID observation with HF Doppler and therefore the TID observed with the HF Doppler could not be verified with GPS data.

Table 4.3 demonstrates comparison values between HF Doppler and GPS TEC results for the four TID events discussed in Section 4.1. Computations reveal that the periods of almost all the TIDs observed with HF Doppler are similar to those observed with GPS. For the event on 06 June 2010 the GPS velocity and period values almost double those of HF Doppler, with the time window of observation having a difference of 54 minutes. However the velocities for the corresponding events are slightly different but with uncertainties included, the velocity ranges overlap. In addition, except for the events on 10 March 2011, the azimuth results show similarities between TIDs observed with HF Doppler and those with GPS. In short, it is reasonable to assume that the TIDs observed on HF Doppler and GPS measurements are of

the same structure. This is an indication that some of the TIDs observed with the HF Doppler radar were seen by other high resolution ionospheric sounding instruments.

4.3 Sources and driving mechanisms

TIDs are instigated by gravity waves when they propagate through the ionosphere. These perturbations are said to be driven by a variety of sources including; solar terminators, auroral electrojets, particle precipitation, magnetic activity, tropospheric weather and mountain turbulence.

4.3.1 TIDs during solar terminator

In Figure 4.6, a scatter plot of the times of occurrence and months of the year of the TID events for years, 2010-2012 is illustrated. Figures 4.6 (a, c, and e) illustrate scatter plots of times of occurrence of MSTIDs while Figures 4.6 (b, d and f) illustrate times of occurrence of LSTIDs. The red solid line and red dotted lines in each figure represent the solar terminator and astronomical twilight lines respectively and demonstrate the relationship between the observed TID events and the passing of the solar terminator. There is a time difference of approximately 2 hours between the twilight line and the terminator lines, both for the morning and the evening times. Therefore, the MSTIDs that were observed within this time window were thought to be excited by the gradients in temperature, and density caused by the solar terminator as it swept across the sky. In 2010, referring to Figure 4.6 (a), there is a significant deviation of the times of occurrence of the observed TID from the sunset terminator for months 6 to 9. The lack of TID observations around the winter sunset terminator might be due to the lack of reflection of the HF Doppler radar sounding frequency by the ionosphere, caused by the decrease in the F2 critical frequency to values below 3.59 MHz, especially during the winter night-times (e.g. Figure 4.1d). A close inspection of Figures 4.6 (a, c, and e) reveals that generally more sunrise terminator induced MSTIDs were observed than the sunset induced MSTIDs. This is in agreement with the findings of the study that was conducted by MacDougall and Jayachandran (2011) who concluded that sunrise terminator TIDs are generally stronger than sunset TIDs. They also noted that the nighttime TIDs did not exhibit any annual variation, a trend not observed from the result presented in Table 4.1

and Figure 4.6. A total of 143 TID events were observed in 2010. Of these, 55 MSTIDs and 11 LSTIDs were observed during the passing of the solar terminator. In 2011, a total of 145 TIDs were analysed and of these, 39 MSTIDs were observed around the passing of the solar terminator and 10 LSTIDs were detected during this time. Ninety-three TID events were analysed in 2012. Approximately 26 MSTIDs and 5 LSTIDs were associated with the passing of solar terminators.

Figure 4.7 provides a summary of possible sources for the observed TID events for the 3-year period. It is evident from Figure 4.6 that during the passing of the solar terminator mostly MSTIDs were observed, but there were times whereby LSTIDs were observed as well. For all 3 years, approximately 33% and 5% of the observed TID events were associated with the sunrise and sunset terminators respectively. It is therefore evident that the sunrise terminator TIDs were more dominant than the sunset TIDs. This is in agreement with the findings obtained by MacDougall and Jayachandran (2011), who observed that solar terminators were responsible for some of the observed the TIDs over middle-latitude F region.

4.3.2 TIDs during magnetic activity

The K index is used to quantify disturbances in the horizontal magnetic field of the Earth between 0 (magnetically quiet) and 9 (magnetically active). To check for geomagnetic activity the local magnetic K index was used to measure the variations in the local magnetic field. For each TID event, approximately 6 hours of K values, around the time of observation of TIDs, were considered. The values of $K > 4$ were chosen to represent the magnetically active periods.

A MSTID, with a period of 24 minutes, was detected moving northwestward on 22 January 2012 at 20:45 - 21:45 LT. A K index value of 4 was observed for the periods 18:00 - 21:00 and 21:00 - 23:59 LT, indicating a geomagnetically active period. This indicated that this MSTID could have been associated with moderate geomagnetic activity.

Two MSTIDs were observed on the 10 March 2011 at 20:00 - 22:00 LT. The K index values observed for this period were 4 and 5 at 18:00 - 21:00 and 21:00 - 23:59 LT respectively an indication of a geomagnetically active period. This was evidence to suggest that the MSTIDs could have been generated by a moderate magnetic storm.

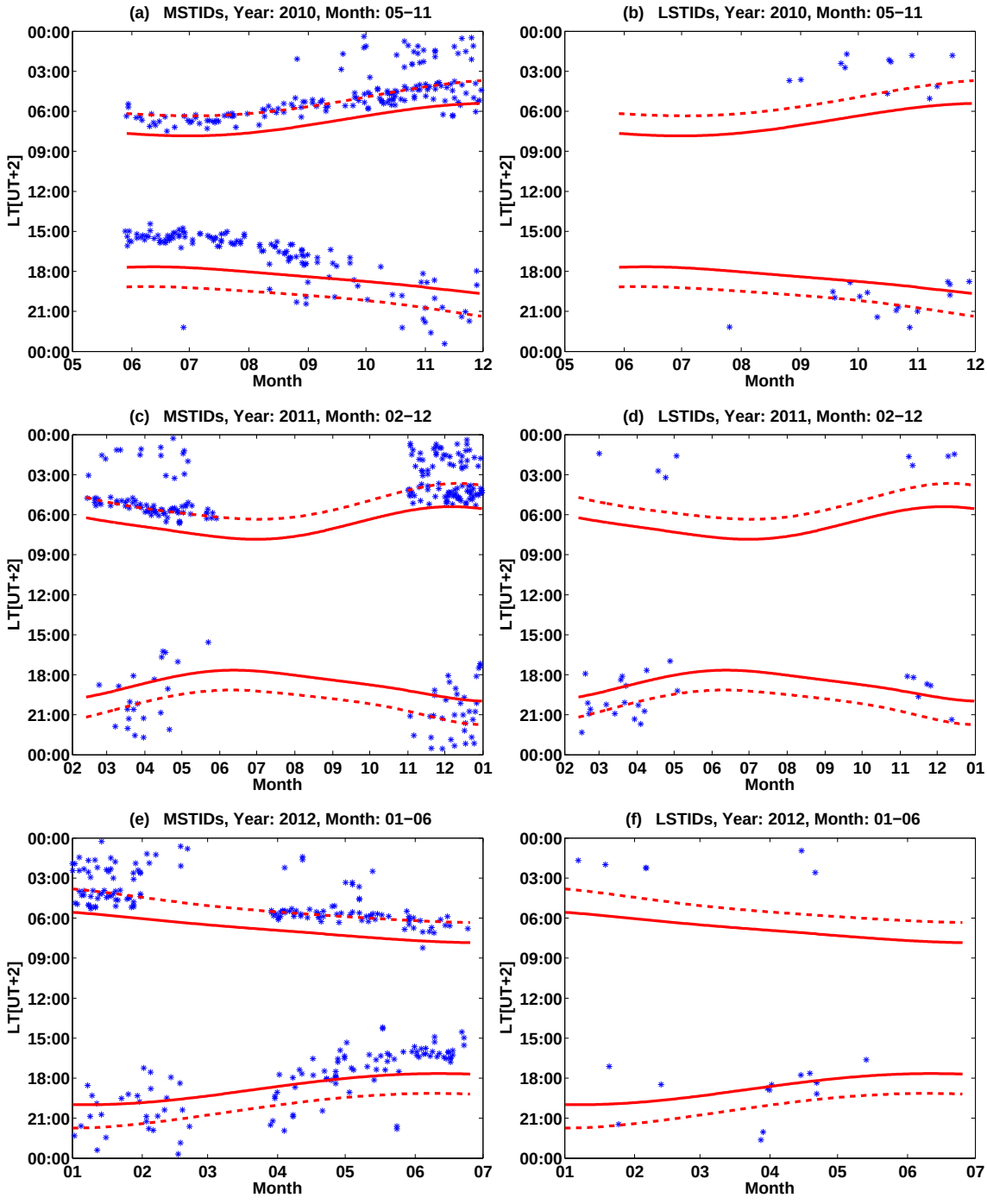

Figure 4.6: These figures represent scatter plots of selected days for selected months of the year to illustrate the observed MSTIDs (a, c & e) and observed LSTIDs (b, d & f). The solid red line represents the sun rise and set times and the red dashed line represents the morning and evening astronomical twilight for the days of observed TIDs.

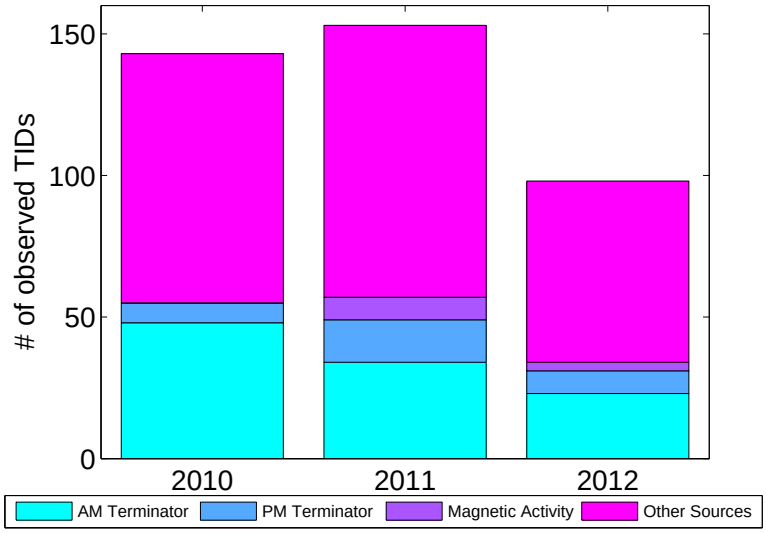

Figure 4.7: TID events associated with solar terminators.

A LSTID, with a period of 72 minutes, was detected on the 16 September 2010 at 17:00 - 22:00 LT, moving westward. The K index values observed for this period were 2, 3 and 1 at 15:00 - 18:00, 18:00 - 21:00 and 21:00 - 23:59 LT respectively, indicating a geomagnetically quiet period. This suggested that the observed LSTID could not have been associated with geomagnetic activity.

A MSTID, with a period of 42 minutes, was observed propagating northwestward on the 06 June 2012 at 15:30 - 17:30 LT. The K index values around the period of observation of the TID were 2 and 2 at 12:00 - 15:00 and 15:00 - 18:00 LT respectively, an indication of a magnetically quiet period. This evidence suggested that the source of this MSTID could not have been a geomagnetic storm as Francis (1974) theorised that MSTIDs can propagate without significant attenuation and changes in their shape, or loss of their coherence no farther than 500-1000 km. Waldock and Jones (1987) also concluded that auroral processes have very little or no part in the generation of MSTIDs at middle latitudes.

Eleven of 381 observed TIDs were associated with enhanced magnetic activity. Most of these 11 structures were observed during the night. This is consistent with the findings by MacDougall and Jayachandran (2011) who concluded that TIDs generated by magnetic activity are mostly observed during nighttime.

4.3.3 Thermospheric body forces

Doppler radar spectrograms often exhibited sudden frequency enhancements, lasting up to approximately 2 hours, in the mornings around the sunrise time and in the evening around sunset times. Figure 4.1 (b) clearly illustrates this during the morning times around 05:00 LT. This effect is also detected in Figure 4.1 (a), in the morning at approximately 04:00 LT. Thermospheric winds, obtained using the HWM07 model, were used to try and understand this phenomenon. Figure 4.8 illustrates a contour plot of meridional wind circulation on the 10 March 2011. During morning hours (00:00 - 03:00 LT) thermospheric winds appear to be moving northward and to higher altitudes reaching a maximum speed of 40 m/s. Between 03:00 and 05:00 LT these thermospheric winds slow down before changing direction at approximately 04:00 LT, and moving southward at approximately 05:00 - 12:00 LT reaching a maximum speed of 40 m/s. From approximately 12:00 LT the wind at this altitude reverses direction again and moves northward reaching maximum speeds of 40 m/s at approximately 20:00 LT. Vertical thermospheric wind profiles at 05:00 LT and 18:00 LT are illustrated in Figure 4.9 (a) to demonstrate wind dynamics at these particular times. According to Jarvis et al. (1998), thermospheric winds play a significant role in plasma density dynamics through change in altitude and hence recombination rate. The northward movement of thermospheric winds pushes the plasma up to higher altitudes encouraging more ionization and hence increasing the ionosphere. The opposite is true for the southward moving winds that push the plasma down, therefore encouraging a higher recombination rate which depletes the ionosphere. The change in wind direction, from moving northward to moving southward, enhances and depletes the ionosphere. Using Equation (2.9), which relates Doppler shifted frequencies to the time change of electron density, one is able to explain the possible mechanism behind the Doppler shift enhancements at approximately 05:00 LT in Figure 4.1. Increase in ionization rate results in the increase of Doppler shifted frequencies whereas an increase in recombination results in the decrease of Doppler shifts.

TIDs observed during the nighttime are also greatly influenced by the dynamics of the thermospheric neutral winds discussed above. Fritts and Alexander (2003) concluded that gravity waves in the thermosphere, which instigate TIDs, have various generating mechanisms such as; topography in the form of mountain waves, convection plumes from lower levels of the atmosphere, wind shear at thermospheric heights, body forcings due to local gravity wave dissipation and momentum flux divergence, and wave-wave interactions. Approximately 77 TIDs observed in 2010 had unidentified sources as well as 88 cases in 2011 and 59 cases in

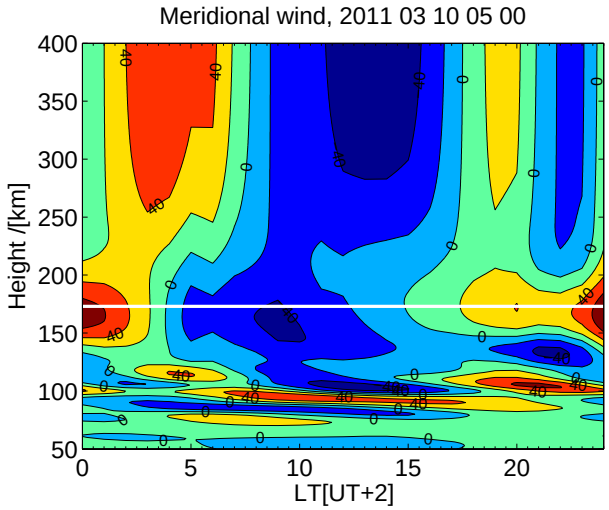

Figure 4.8: Contour plot of Meridional wind speeds in m/s as function of time and altitude for the 10 March 2011. The horizontal white line represents the mean radar signal reflection altitude of 173 km.

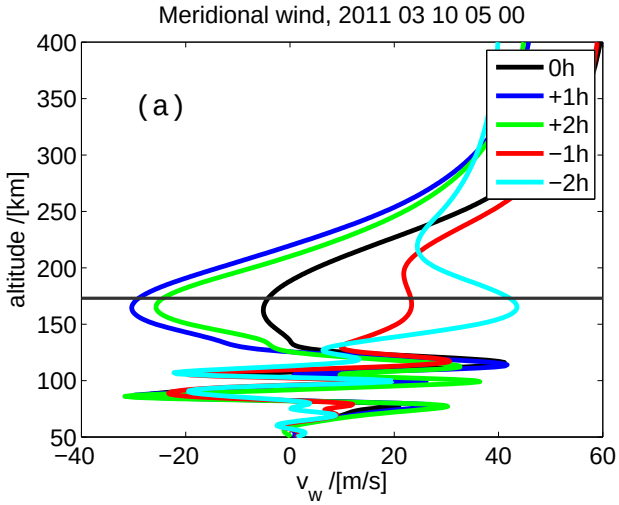

Figure 4.9: Meridional wind speeds as a function of altitude at the time of observation of TIDs. Dark horizontal line indicates an average reflection height of the HF Doppler radar signal. The graphs in color indicate hourly vertical meridional wind profiles around the hour of observation of TID, labelled “0h”(black profile).

2012. These TIDs, with unknown sources, could be linked to the gravity wave generating mechanisms mentioned above.

A further investigation into the possible sources of TIDs that were not associated with magnetic activity was conducted using thermospheric neutral winds, modeled with HWM07. The model clearly picked up the diurnal circulation of the wind but could not resolve the medium scale and large scale perturbations which could happen any time during the day. The same set back was encountered with the International Reference Ionosphere (IRI) model. The temporal and spatial resolution of these models was found lacking when exploring sources of TIDs observed in this study.

A more detailed study of gravity waves generated by these mechanisms, with the use of better atmospheric models and other high resolution atmospheric sounders such as LIDAR and airglow imagers, is needed to better establish the exciting mechanisms. The MSTIDs that were observed on 16 November 2010 19:00 - 22:00 LT and on the 06 June 2012 15:30 - 17:30 LT, respectively , could have been generated by any of the forcings mentioned above. These could most probably be associated with thermospheric body forces created from the dissipation of primary gravity waves from convection plumes (Alexander, 1995).

4.4 Discussion and Comparison with Previous Reports

The research work presented in this thesis is an assessment of approximately 3 years of data comprising of some 381 captured events from the South African HF Doppler dataset. This study is an extension of similar studies by Chum et al. (2012) and Sindelarova et al. (2012), and is more comprehensive and focused on local South African conditions.

During the course of this study a triangular HF Doppler radar system located in the Western Cape of South Africa, with transmitters in Arniston ($34^{\circ}36'9''S$, $20^{\circ}18'10''E$), Cape Town ($33^{\circ}56'16''S$, $18^{\circ}28'15''E$) and Worcester ($33^{\circ}38'42''S$, $19^{\circ}26'37''E$), and a receiver in Hermanus ($34^{\circ}25'30''S$, $19^{\circ}13'30''E$), was utilized to gather primary data. Wavelet analysis (Section 3.2) was the main digital signal processing technique utilized to obtain spectral components of the data because of its ability to resolve time information of each spectral component of the time series. The HF Doppler dataset was analysed for MSTIDs (periods < 40 minutes and speeds < 400 m/s) and LSTIDs (periods >= 40 minutes and speeds >=

400 m/s). The analysis was divided into daytime (AM: 00:00 - 11:59 LT) and nighttime (PM: 12:00 - 23:59 LT) observations. The statistical summary (refer to Table 4.1) of the observed TIDs revealed some seasonal dependencies for both MSTIDs and LSTIDs. The occurrence rate of MSTIDs observed during autumn and spring is higher than during winter and summer. Daytime MSTIDs were generally faster than the nighttime MSTIDs. The daytime MSTIDs appeared to be propagating southwestward whereas the nighttime MSTIDs propagated in a more southward direction. Some seasonal variation is apparent in daytime and nighttime horizontal averaged speeds of MSTIDs; those in winter have a fastest mean speed of 205.4 ± 51.1 m/s, those in autumn and spring have an average speed of 186.3 ± 61.4 m/s and those in summer have slowest mean speed of 175.3 ± 34.3 m/s. The occurrence rate of LSTIDs demonstrates apparent seasonal dependency; the rate is much smaller in summer compared to autumn and spring. More LSTIDs were observed during nighttime and, for autumn and spring, these were generally slower than the daytime ones. In summer the nighttime LSTIDs had an average speed of 640.9 ± 63.1 m/s whereas the daytime LSTIDs propagated with a mean speed of approximately 607 m/s. LSTIDs observed in spring were generally faster than those in autumn and summer. The propagation direction of the nighttime LSTIDs also revealed seasonal differences. The seasonal average propagation directions of the nighttime LSTIDs in summer, autumn and spring are $195 \pm 74^\circ$, $156 \pm 64^\circ$, and $170 \pm 76^\circ$, respectively. This seasonal variation of the propagation direction is most likely due to the different seasonal geographic locations of the solar terminator at dusk. The sources of the observed TIDs were determined and proposed.

A similar study was conducted by Chum et al. (2012) over South Africa and Europe for the period between June 2010 and May 2011. For South Africa, their study illustrated that the winter MSTIDs are faster that the summer MSTIDs. This is in good agreement with the results observed from Table 4.1. The average seasonal velocities they reported are slightly lower than velocities obtained in this study. The reason for this could be that the thermospheric wind velocities effect was not considered in this study when calculating TID velocities. Chum et al. (2012) also noted that the poleward propagation of TIDs in the northern hemispheric summer is usually associated with the intense convective activity in the equatorial troposphere. This confirms the poleward preferred direction of propagation of TIDs observed during summer as seen in Table 4.1. On the other hand, in the middle-latitude, Shiokawa et al. (2009) reported equatorward and westward propagation of nighttime MSTIDs for all seasons. Another study by Kotake and Otsuka (2007) also concluded that the MSTIDs had a general equatorward preferred direction of travel. This is in contrast with what is ob-

served in Table 4.1. It should be noted that although Shiokawa et al. (2009) and Kotake and Otsuka (2007) also conducted their studies over middle-latitudes but different longitudes, there could be different driving forces of TIDs. For example both locations (i.e. China and Southern California) are prone to earthquakes which also contribute towards TID activity unlike in South Africa, where there are usually no earthquakes.

An attempt was made to link the observed TIDs to AGW sources such as magnetic storms and solar terminators of a total of 381 events observed between May 2010 and June 2012, approximately 38% of the TID events were observed around the passing of the solar terminator. This gave an indication that these TIDs could have been triggered by the solar terminators. The sunrise terminator associated MSTIDs were more dominant than the sunset terminator associated MSTID, both in quantity and speeds. Galushko and Paznukhov (1998) studied TIDs generated by the moving solar terminator using an incoherent scatter radar. In his study, he also concluded that the sunrise solar terminator generated TIDs were more dominant than the TIDs generated by the sunset solar terminator. This finding was further confirmed by other authors (e.g. Afraimovich et al., 2009, 2010; MacDougall and Jayachandran, 2011).

Approximately 3% of the observed TIDs were linked to the occurrence of magnetic storms. Most of these LSTIDs were observed during the night. This is consistent with the findings on the study by MacDougall and Jayachandran (2011) who also confirmed that LSTIDs associated with geomagnetic activity are mostly observed during nighttime. No such trend was observed with the LSTIDs. Several other authors have also linked the occurrence of LSTIDs to geomagnetic storms (e.g. Ding et al., 2007; Perevalova et al., 2008). The small percentage of TIDs associated with geoamgnetic activity could be attributed to the fact that the period (2010 - 2012) for which the data were analysed was a lower solar cycle period, with a lesser number of significant geoeffective space weather events, when compared to the previous one. For example, during this period only 9 strong magnetic storms (with the $D_{st} < -100$nT) were observed, comparing to 2000, a high solar cycle period, when 12 strong-to-intense magnetic storms occurred within one year. It is, therefore, reasonable to assume that the above mentioned percentage could be higher for the higher solar cycle, as magnetic storms are significant source of TIDs.

The rest of the observed TID events, approximately 59%, could not be directly linked to either magnetic storm activity or solar terminators. Atmospheric models such as HWM07 and IRI were attempted to model AGW excited by forcings in the thermosphere. This attempt was unsuccessful mainly because the spatial and temporal resolutions of these models were found

lacking. Neither atmospheric data nor models were available to study auroral activity in the Southern Hemisphere. Auroral substorms are also thought to excite AGW which can generate TIDs at middle latitudes(e.g. Waldock and Jones, 1987).

The mean reflection height of the Hermanus HF Doppler radar signal is 173 km. This altitude is in the thermospheric range (approximately 120 - 250 km) within which AGW are said to dissipate, causing horizontal thermospheric body forces (e.g. convective plumes, wind shear, wave-wave interactions etc) that are large enough to generate secondary AGW and LSTIDs (Vadas and Liu, 2009). This could account for the number of LSTIDs detected by the HF Doppler radar during magnetically and auroral quiet time (Šauli and Boška, 2001). A study by Zhou et al. (2012) confirmed the generation of LSTIDs by secondary AGW from thermospheric body forces created from the dissipation of primary AGW via deep tropospheric convection. While investigating the sources of TIDs, using a Doppler radar called TIDDBIT, Vadas and Crowley (2010) identified as many as 46% of the observed TIDs to be associated with secondary gravity waves excited by thermospheric body forces. By making use of a high resolution thermosphere ionosphere mesosphere electrodynamic general circulation model (TIME-GCM) in conjunction with the ray trace model, they were able to simulate thermospheric body forces from convention plumes. On the basis of the dispersion relation, Hines (1960) and Waldock and Jones (1984) showed that TIDs that are associated with a tropospheric jet flow occur in the F-region in the form of a wave packet with quasi-monochromatic oscillations, the period of which is a function of inclination angle of the wave vector during the propagation of the wave from the source to the place of observation in the F-region. Therefore, taking into account results from these studies it is reasonable to suspect that some of the 59% TIDs (MSTIDs and LSTIDs combined) observed could be associated with thermospheric body forces.

4.5 Summary

This chapter has investigated and discussed the propagation characteristics of TIDs over the southwestern region of South Africa using the HF Doppler radar network. A database of approximatelly 3 years was utilised in the study. The study revealed that the MSTIDs are more frequently observed than the LSTIDs, consistent with many past studies of TIDs. The daytime TIDs are generally faster than the nighttime, for both MSTIDs and LSTIDs. MSTIDs have a south-southwest preferred direction of travel whereas the LSTIDs often propagate

southwards. The TIDs for 22 Jan 2012, 10 Mar 2011, 16 Sep 2010 and 06 Jun 2012 observed with HF Doppler were mostly validated with GPS data. Thirty-eight percent of the observed TIDs were associated with the passing of the solar terminator. Approximately three percent of the observed TIDs were associated with geomagnetic activity, and approximately fifty-nine percent of the observed TIDs had unknown sources of origin. An attempt to identify the sources of origin of the rest of the observed TIDs was made using atmospheric models such as HWM07 and IRI but to no avail, because of the inadequate spatial and temporal resolutions of these models.

Chapter 5

Concluding Remarks and Future Perspectives

This research aimed to achieve the three primary objectives provided in Chapter 1, and repeated here for ease of reference.

- Identify TIDs using the HF Doppler radar and determine their propagation characteristics namely; the speed, period, wavelength and direction of propagation.
- Provide statistical information of TIDs' propagation properties such as spatial and temporal dependances.
- Determine the possible sources and driving mechanisms of the observed TIDs.

Using an HF Doppler radar dataset of almost three years, TIDs were successfully identified and their speeds, periods, wavelengths and azimuths calculated. Statistical summary on speed and direction of propagation of the observed TIDs was performed. The winter medium scale travelling ionospheric disturbances (MSTIDs) observed are generally faster than the summer MSTIDs. For all seasons, the MSTIDs had a preferred south-southwest direction of propagation. Most of the large scale travelling ionospheric disturbances (LSTIDs) were observed during the night and of these, the spring LSTIDs were fastest when compared to autumn and summer LSTIDs. The general direction of travel of the observed LSTIDs is south-southeast. Total Electron Content (TEC), derived from Global Positioning System (GPS) measurements, were used to validate some of the TID results

obtained from the HF Doppler data. The Horizontal Wind Model (HWM07), magnetic K index, and solar terminators were used to determine the possible sources of the observed TIDs. Only 41% of the observed TIDs were successfully linked to their possible sources of excitation..

5.1 Future Work

It is recognized that there are some topics covered in this work which have not been fully explored and could form the basis of further research. The research, as presented, could be extended to explore other sources of observed TIDs by utilizing other suitable datasets (e.g LIDAR, TIME-GCM, etc.). The study can be improved upon if:

The HF Doppler radar is slightly modified. The HF Doppler radar utilized a single continuous operating frequency of 3.59 MHz. Except during winter, this frequency works well during the morning and evening times when the ionosphere is still thinner and the *D*-region is absent. At around midday the *D*-region absorbs most/all of the radar signal, resulting in faint/no signals being received at the receiver. This could be overcome by modifying the radar to operate on a second frequency of approximately 8 MHz or more. An additional operating frequency of approximately 2 MHz would ensure uninterrupted TIDs investigation for the entire day, even during winter nighttimes when the critical frequency of the F-region is much smaller than 3.59 MHz. This modification will also allow for the vertical component of propagation of the TIDs to be determined.

Other datasets are utilized. Some of the observed TIDs could have been excited by auroral processes. Further investigation on the link between these sources and the observed TID events is needed. Other atmospheric sounding instruments such as the light detection and ranging (LIDAR) and airglow imager, jointly with a higher resolution atmospheric model such as TIME-GCM, are needed to better ascertain sources of TIDs associated with thermospheric body forces.

In closing, the understanding of the dynamics of the ionosphere is an essential part of radio communication. This research has formed a basis on which the ionospheric models and radio communication over South Africa can be improved or developed.

References

Afraimovich, E.: Dynamics and anisotropy of travelling ionospheric disturbances as deduced from transionospheric sounding data. I-Statistical angle-of-arrival and Doppler method (SADM), Preprint, pp. 5–95, 1995.

Afraimovich, E.: Statistical Method for determining characteristics of the dynamics of the radio signal interference pattern, Acta Geodaetica et Geophysica Hungarica, 32, 461–468, 1997.

Afraimovich, E.: The use of the international GPS network as the global detector (GLOBDET) simultaneously observing sudden ionospheric disturbances, Earth, Planets and Space, 52, 1077–1082, 2000.

Afraimovich, E. and Voyeikov, S.: Ionosphere wave packets excited by the solar terminator: AGW or MHD origin?, in: Progress In Electromagnetics Research Symposium Proceedings, Moscow, Rassia, vol. 0, pp. 233–237, 2009.

Afraimovich, E., Palamartchouk, K., and Perevalova, N.: GPS radio interferometry of travelling ionospheric disturbances, Journal of Atmospheric and Solar-Terrestrial Physics, 60, 1205–1223, 1998.

Afraimovich, E. L., Boitman, O. N., Zhovty, E. I., Kalikhman, a. D., and Pirog, T. G.: Dynamics and anisotropy of traveling ionospheric disturbances as deduced from transionospheric sounding data, Radio Science, 34, 477–487, 1999.

Afraimovich, E. L., Perevalova, N. P., and Voyeikov, S. V.: Traveling wave packets of total electron content disturbances as deduced from global GPS network data, Journal of Atmospheric and Solar-Terrestrial Physics, 65, 1245–1262, 2003.

Afraimovich, E. L., Edemskiy, I. K., Voeykov, S. V., Yasyukevich, Y. V., and Zhivetiev, I. V.: The first GPS-TEC imaging of the space structure of MS wave packets excited by the solar terminator, Annales Geophysicae, 27, 1521–1525, 2009.

Afraimovich, E. L., Edemsky, I. K., Voeykov, S. V., Yasukevich, Y. V., and Zhivetiev, I. V.: MHD nature of ionospheric wave packets generated by the solar terminator, Geomagnetism and Aeronomy, 50, 79–95, 2010.

Alexander, M.: The gravity wave response above deep convection in a squall line simulation, Journal of the Atmospheric Sciences, 52, 2212–2226, 1995.

Amabayo, E. B., McKinnell, L.-A., and Cilliers, P. J.: Ionospheric response over South Africa to the geomagnetic storm of 11-13 April 2001, Journal of Atmospheric and Solar-Terrestrial Physics, 84-85, 62–74, 2012.

Andrews, D. G.: An introduction to atmospheric physics, Cambridge University Press, 2010.

Banks, P. M. and Kockarts, G.: Aeronomy, Academic Press (New York), 1 edn., 1973.

Beer, T.: Atmospheric waves, Adam Hilger Ltd, 1974.

Bloomfield, D. S., McAteer, R. T. J., Lites, B. W., Judge, P. G., Mathioudakis, M., and Keenan, F. P.: Wavelet phase coherence analysis: application to a Quiet-Sun magnetic element, The Astrophysical Journal, 617, 623–632, 2004.

Bristow, W. A. and Greenwald, R. A.: Multiradar observations of medium-scale acoustic gravity waves using the Super Dual Auroral Radar Network, Journal of Geophysical Research, 101, 24 499–24 511, 1996.

Bristow, W. A., Greenwald, R. A., and Samson, J. C.: Identification of high-latitude acoustic gravity wave sources using the Goose Bay HF Radar, Journal of Geophysical Research, 99, 319–331, 1994.

Campbell, W. H.: Introduction to geomagnetic fields, Cambridge University Press, 1997.

Campbell, W. H.: Earth Magnetism: a guided tour through magnetic fields, Harcourt/Academic Press, 2001.

Chane-Ming, F., Guest, F., and Karoly, D.: Gravity waves observed in temperature, wind and ozone data over Macquarie Island, Australian Meteorological Magazine, 52, 2003.

Cheng, K., Huang, Y.-N., and Chen, S.-W.: Travelling ionospheric disturbances detected during the solar eclipse of 24 October 1995, Journal of Terrestrial, Atmospheric and Oceanic Sciences, 8, 213–220, 1997.

Chum, J., Laštovička, J., Šindelárová, T., Burešová, D., and Hruška, F.: Peculiar transient phenomena observed by HF Doppler sounding on infrasound time scales, Journal of Atmospheric and Solar-Terrestrial Physics, 70, 866–878, 2008.

Chum, J., Šindelárová, T., Laštovička, J., Hruška, F., Burešová, D., and Baše, J.: Horizontal velocities and propagation directions of gravity waves in the ionosphere over the Czech Republic, Journal of Geophysical Research, 115, 1–13, 2010.

Chum, J., Athieno, R., Baše, J., Burešová, D., Hruška, F., Laštovička, J., McKinnell, L.-A., and Šindelárová, T.: Statistical investigation of horizontal propagation of gravity waves in the ionosphere over Europe and South Africa, Journal of Geophysical Research, 117, 1–13, 2012.

Chun-Lin, L.: A Tutorial of the Wavelet Transform, NTUEE, Taiwan, 2010.

Cowling, D., Webb, H., and Yeh, K.: Group rays of internal gravity waves in a wind-stratified atmosphere, Journal of Geophysical Research, 76, 213–220, 1971.

Crowley, G. and Rodrigues, F. S.: Characteristics of traveling ionospheric disturbances observed by the TIDDBIT sounder, Radio Science, 47, 2012.

Crowley, G., Jones, T., Robinson, T., Wade, N., and Holt, O.: Determination of the vertical neutral temperature and wind profiles using EISCAT and HF Doppler radar, Journal of Atmospheric and Terrestrial Physics, 46, 501–507, 1984.

Davies, K.: Ionospheric Radio, P. Peregrinus on behalf of the Institution of Electrical Engineers (London, U.K.), 31 edn., 1989.

Davis, M. J.: On polar substorms as the source of large-scale traveling ionospheric disturbances, Journal of Geophysical Research, 76, 4525–4533, 1971.

Davis, M. J. and da Rosa, A. V.: Traveling ionospheric disturbances originating in the auroral oval during polar substorms, Journal of Geophysical Research, 74, 5721–5735, 1969.

Davis, T. N. and Sugiura, M.: Auroral electrojet activity index AE and its universal time variations, Journal of Geophysical Research, 71, 785–801, 1966.

Ding, F., Wan, W., Ning, B., and Wang, M.: Large-scale traveling ionospheric disturbances observed by GPS total electron content during the magnetic storm of 29-30 October 2003, Journal of Geophysical Research, 112, A06 309, 2007.

Drob, D. P., Emmert, J. T., Crowley, G., Picone, J. M., Shepherd, G. G., Skinner, W., Hays, P., Niciejewski, R. J., Larsen, M., She, C. Y., Meriwether, J. W., Hernandez, G., Jarvis, M. J., Sipler, D. P., Tepley, C. a., O'Brien, M. S., Bowman, J. R., Wu, Q., Murayama, Y., Kawamura, S., Reid, I. M., and Vincent, R. A.: An empirical model of the Earth's horizontal wind fields: HWM07, Journal of Geophysical Research, 113, A12 304, 2008.

Francis, S.: Acoustic-gravity modes and large-scale traveling ionospheric disturbances of a realistic, dissipative atmosphere, Journal of Geophysical Research, 78, 2278–2301, 1973.

Francis, S.: Theory of medium-scale traveling ionospheric disturbances, Journal of Geophysical Research, 79, 5245–5260, 1974.

Francis, S. H.: Global propagation of atmospheric gravity waves - A review, Journal of Atmospheric and Terrestrial Physics, 37, 1011–1054, 1975.

Fritts, D. D. C. and Alexander, M.: Gravity wave dynamics and effects in the middle atmosphere, Reviews of Geophysics, 41, 1003, 2003.

Galushko, V. and Paznukhov, V.: Incoherent scatter radar observations of AGW/TID events generated by the moving solar terminator, Annales Geophysicae, 16, 821–827, 1998.

Georges, T.: HF Doppler studies of traveling ionospheric disturbances, Journal of Atmospheric and Terrestrial Physics, 30, 735–746, 1968.

Hajkowicz, L.: A global study of large scale travelling ionospheric disturbances (TIDS) following a step-like onset of auroral substorms in both hemispheres, Planetary and Space Science, 38, 913–923, 1990.

Hannah, B. M.: Modelling and simulation of GPS multipath propagation, Ph.D. thesis, 2001.

He, L. and Dyson, P.: Medium-Scale travelling ionospheric disturbances studied with the TIGER HF SuperDARN radar, in: Proceedings of the workshop on the applications of Radio Science, pp. 1–6, 2002.

Hedin, A.: MSIS-86 thermospheric model, Journal of Geophysical Research, 92, 4649–4662, 1987.

Hedin, A. and Biondi, M.: Revised global model of thermosphere winds using satellite and ground-based observations, Journal of Geophysical Research: Space Physics (1978–2012), 96, 7657–7688, 1991.

Hedin, A., Spencer, N., and Killeen, T.: Empirical global model of upper thermosphere winds based on Atmosphere and Dynamics Explorer satellite data, Journal of Geophysical Research: Space Physics (1978–2012), 93, 9959–9978, 1988.

Hedin, A., Fleming, E., Manson, A., Schmidlin, F., Avery, S., Clark, R., Franke, S., Fraser, G., Tsuda, T., Vial, F., and Vincent, R.: Empirical wind model for the upper, middle and lower atmosphere, Journal of Atmospheric and Terrestrial Physics, 58, 1421–1447, 1996.

Hernández-Pajares, M., Juan, J. M., and Sanz, J.: Medium-scale traveling ionospheric disturbances affecting GPS measurements: Spatial and temporal analysis, Journal of Geophysical Research, 111, A07S11, 2006.

Hernández-Pajares, M., Juan, J. M., Sanz, J., and Aragón-Àngel, A.: Propagation of medium scale traveling ionospheric disturbances at different latitudes and solar cycle conditions, Radio Science, 47, 2012.

Hines, C.: Internal atmospheric gravity waves at ionospheric heights, Canadian Journal of Physics, 38, 1441–1481, 1960.

Hines, C.: The saturation of gravity waves in the middle atmosphere. Part II: Development of Doppler-spread theory, Journal of Atmospheric Sciences, 48, 1361–1379, 1991.

Hodges, R.: Generation of turbulence in the upper atmosphere by internal gravity waves, Journal of Geophysical Research, 72, 3455–3458, 1967.

Hofmann-Wellenhof, B., Lichtenegger, H., and Collins, J.: Global Positioning System: Theory and practice, Springer Wien New York, 4 edn., 1997.

Hunsucker, R. D.: Atmospheric gravity waves generated in the high-latitude ionosphere: A review, Reviews of Geophysics, 20, 293–315, 1982.

Hunsucker, R. D. and Hargreaves, J. K.: The high-latitude ionosphere and its effects on radio propagation, Cambridge University Press, Cambridge, 2002.

Jarvis, M., Jenkins, B., and GA, R.: Southern hemisphere observations of a long-term decrease in F region altitude and thermospheric wind providing possible evidence for global

thermospheric cooling, Journal of Geophysical Research: Space Physics, 103, 20 774–20 787, 1998.

Kotake, N. and Otsuka, Y.: Statistical study of medium-scale traveling ionospheric disturbances observed with the GPS networks in Southern California, Earth, Planets, and Space, 59, 95–102, 2007.

Kutiev, I., Marinov, P., Fidanova, S., and Warnant, R.: Modeling medium-scale TEC structures, observed by Belgian GPS receivers network, Advances in Space Research, 43, 1732–1739, 2009.

Lane, T., Reeder, M., and Clark, T.: Numerical modeling of gravity wave generation by deep tropical convection, Journal of the Atmospheric Sciences, 58, 1249–1274, 2001.

Lang, Â.: The Cambridge Encyclopedia of the Sun, The Cambridge Encyclopedia of the Sun, 2001.

Larson, K. M., Small, E. E., Gutmann, E., Bilich, A., Axelrad, P., and Braun, J.: Using GPS multipath to measure soil moisture fluctuations: initial results, GPS Solutions, 12, 173–177, 2007.

Lau, K. and Weng, H.: Climate signal detection using wavelet transform: How to make a time series sing, Bulletin of the American Meteorological Society, 76, 2391–2402, 1995.

Lee, D. and Yamamoto, A.: Wavelet analysis: Theory and applications, Hewlett Packard journal, 45, 44–52, 1994.

Liu, H., Lühr, H., and Watanabe, S.: A solar terminator wave in thermospheric wind and density simultaneously observed by CHAMP, Geophysical Research Letters, 36, L10 109, 2009.

Liu, P.: Wavelet spectrum analysis and ocean wind waves, Wavelets in geophysics, 4, 151–166, 1994.

MacDougall, J. and Jayachandran, P.: Solar terminator and auroral sources for traveling ionospheric disturbances in the midlatitude F region, Journal of Atmospheric and Solar-Terrestrial Physics, 73, 2437–2443, 2011.

MacDougall, J., Abdu, M., Batista, I., Fagundes, P., Sahai, Y., and Jayachandran, P.: On the production of traveling ionospheric disturbances by atmospheric gravity waves, Journal of Atmospheric and Solar-Terrestrial Physics, 71, 2013–2016, 2009.

Mallat, S. G.: A wavelet tour of signal processing, Academic Press (San Diego), 1998.

McNamara, L. F.: The ionosphere: Communications, surveillance, and direction finding, Krieger Pub. Co., original edn., 1991.

Mercier, Â.: Observations of atmospheric gravity waves by radiointerferometry, Journal of Atmospheric and Terrestrial Physics (ISSN 0021-9169), 48, 605–624, 1986.

Misra, P. and Enge, P.: Global positioning system, signals, measurements, and performance, Massachusetts: Ganga-Jamuna Press, 3 edn., 2006.

Montenbruck, O., Hugentobler, U., Dach, R., Steigenberger, P., and Hauschild, A.: Apparent clock variations of the Block IIF-1 (SVN62) GPS satellite, GPS solutions, 16, 303–313, 2012.

Munro, G.: Travelling ionospheric disturbances in the F region, Australian Journal of Physics, 11, 91–112, 1958.

Munro, G. H.: Travelling disturbances in the ionosphere, Proceedings of the Royal Society A: Mathematical, Physical and Engineering Sciences, 202, 208–223, 1950.

Nava, B., Radicella, S., Leitinger, R., and Coïsson, P.: Use of total electron content data to analyze ionosphere electron density gradients, Advances in Space Research, 39, 1292–1297, 2007.

Otsuka, Y.: Geomagnetic conjugate observations of medium-scale traveling ionospheric disturbances at midlatitude using all-sky airglow imagers, Geophysical Research Letters, 31, L15 803, 2004.

Perevalova, N. P., Afraimovich, E. L., Voeykov, S. V., and Zhivetiev, I. V.: Parameters of large-scale TEC disturbances during the strong magnetic storm on 29 October 2003, Journal of Geophysical Research, 113, A00A13, 2008.

Petrova, I., Bochkarev, V., and Latipov, R.: Application of HF Doppler measurements for the investigation of internal atmospheric waves in the ionosphere, Advances in Space Research, 44, 685–692, 2009.

Price, R. E.: Travelling disturbances in the ionosphere, Nature, 172, 115–116, 1953.

Rawer, K.: Wave propagation in the ionosphere, Kluwer Academic, 5 edn., 1993.

Ripka, P.: Advances in fluxgate sensors, Sensors and Actuators A: Physical, 106, 8–14, 2003.

Rishbeth, H.: Thermospheric targets, Eos, Transactions American Geophysical Union, 88, 189–193, 2007.

Rishbeth, H. and Garriott, O. K.: Introduction to ionospheric physics, Academic Press, 1 edn., 1969.

Rostoker, G., Akasofu, S.-I., Foster, J., Greenwald, R., Kamide, Y., Kawasaki, K., Lui, A., McPherron, R., and Russell, C.: Magnetospheric substorms- Definition and signatures, Journal of Geophysical Research, 85, 1663–1668, 1980.

Saha, K.: The Earth's Atmosphere: Its Physics and Dynamics, Springer, 2008.

Sardón, E. and Zarraoa, N.: Estimation of total electron content using GPS data: How stable are the differential satellite and receiver instrumental biases?, Radio science, 32, 1899–1910, 1997.

Schmidt, M. and Schuh, H.: Abilities of Wavelet Analysis for investigating short-period variation of Earth rotation, IERS Technical Note, 2000.

Shiokawa, K., Otsuka, Y., and Ogawa, T.: Propagation characteristics of nighttime mesospheric and thermospheric waves observed by optical mesosphere thermosphere imagers at middle and low, Earth Planets Space, 61, 479–491, 2009.

Sindelarova, T., Mosna, Z., Buresova, D., Chum, J., McKinnell, L.-A., and Athieno, R.: Observations of wave activity in the ionosphere over South Africa in geomagnetically quiet and disturbed periods, Advances in Space Research, 50, 182–195, 2012.

Somsikov, V.: On mechanisms for the formation of atmospheric irregularities in the solar terminator region, Journal of Atmospheric and Terrestrial Physics, 57, 75–83, 1995.

Song, Q., Ding, F., Wan, W., Ning, B., Liu, L., Zhao, B., Li, Q., and Zhang, R.: Statistical study of large-scale traveling ionospheric disturbances generated by the solar terminator over China, Journal of Geophysical Research: Space Physics, 118, 4583–4593, 2013.

Ta, J. L.: Global Positioning System, Ph.D. thesis, California State University, 2011.

Torrence, C. and Compo, G. P.: A Practical Guide to Wavelet Analysis, Bulletin of the American Meteorological Society, 79, 61–78, 1995.

Vadas, S. L.: Thermospheric responses to gravity waves: Influences of increasing viscosity and thermal diffusivity, Journal of Geophysical Research, 110, D15 103, 2005.

Vadas, S. L.: Horizontal and vertical propagation and dissipation of gravity waves in the thermosphere from lower atmospheric and thermospheric sources, Journal of Geophysical Research, 112, A06 305, 2007.

Vadas, S. L. and Crowley, G.: Sources of the traveling ionospheric disturbances observed by the ionospheric TIDDBIT sounder near Wallops Island on 30 October 2007, Journal of Geophysical Research, 115, A07 324, 2010.

Vadas, S. L. and Fritts, D. C.: Influence of solar variability on gravity wave structure and dissipation in the thermosphere from tropospheric convection, Journal of Geophysical Research, 111, A10S12, 2006.

Vadas, S. L. and Liu, H.-l.: Generation of large-scale gravity waves and neutral winds in the thermosphere from the dissipation of convectively generated gravity waves, Journal of Geophysical Research, 114, A10 310, 2009.

Valladares, C. E. and Hei, M. a.: Measurement of the characteristics of TIDs using small and regional networks of GPS receivers during the campaign of 17-30 July of 2008, International Journal of Geophysics, 2012, 1–14, 2012.

Valladares, C. E., Villalobos, J., Hei, M. a., Sheehan, R., Basu, S., MacKenzie, E., Doherty, P. H., and Rios, V. H.: Simultaneous observation of traveling ionospheric disturbances in the Northern and Southern Hemispheres, Annales Geophysicae, 27, 1501–1508, 2009.

Vincent, R.: Gravity wave coupling from below: A review, in: CAWSES: Selected papers from the 2007 Kyoto symposium, 1960, pp. 279–293, 2009.

Vincent, R. and Reid, I.: HF Doppler measurements of mesospheric gravity wave momentum fluxes, Journal of the Atmospheric Sciences, 40, 1321–1333, 1983.

Šauli, P. and Boška, J.: Tropospheric events and possible related gravity wave activity effects on the ionosphere, Journal of Atmospheric and Solar-Terrestrial Physics, 63, 945–950, 2001.

Waldock, J. and Jones, T.: The effects of neutral winds on the propagation of medium-scale atmospheric gravity waves at mid-latitudes, Journal of Atmospheric and Terrestrial Physics, 46, 217–231, 1984.

Waldock, J. and Jones, T.: HF Doppler observations of medium-scale travelling ionospheric disturbances at mid-latitudes, Journal of Atmospheric and Terrestrial Physics, 48, 245–260, 1986.

Waldock, J. and Jones, T.: Source regions of medium scale travelling ionospheric disturbances observed at mid-latitudes, Journal of Atmospheric and Terrestrial Physics, 49, 105–114, 1987.

Zhou, C., Zhao, Z., Yang, G., Chen, G., Hu, Y., and Zhang, Y.: Evidence of low-latitude daytime large-scale traveling ionospheric disturbances observed by high-frequency multistatic backscatter sounding system during a geomagnetically quiet period, Journal of Geophysical Research, 117, 1–8, 2012.